J. Fluid Mech. (2010), *vol.* 645, *pp.* 211–254.
doi:10.1017/S0022112009992606

A posteriori study using a DNS database describing fluid disintegration and binary-species mixing under supercritical pressure: heptane and nitrogen

EZGI S. TASKINOGLU[1] AND JOSETTE BELLAN[1,2]†

[1]California Institute of Technology, Pasadena, CA 91125, USA

[2]Jet Propulsion Laboratory, California Institute of Technology, Pasadena, CA 91109, USA

(Received 15 April 2009; revised 29 September 2009; accepted 30 September 2009; first published online 9 February 2010)

A large eddy simulation (LES) *a posteriori* study is conducted for a temporal mixing layer which initially contains different species in the lower and upper streams and in which the initial pressure is larger than the critical pressure of either species. A vorticity perturbation, initially imposed, promotes roll-up and a double pairing of four initial spanwise vortices to reach a transitional state. The LES equations consist of the differential conservation equations coupled with a real-gas equation of state, and the equations utilize transport properties depending on the thermodynamic variables. Unlike all LES models to date, the differential equations contain, additional to the subgrid-scale (SGS) fluxes, a new SGS term denoted a 'pressure correction' (p correction) in the momentum equation. This additional term results from filtering the Navier–Stokes equations and represents the gradient of the difference between the filtered p and p computed from the filtered flow field. A previous *a priori* analysis, using a direct numerical simulation (DNS) database for the same configuration, found this term to be of leading order in the momentum equation, a fact traced to the existence of regions of high density-gradient magnitude that populated the entire flow; in that study, the appropriateness of several SGS-flux models was assessed, and a model for the p-correction term was proposed.

In the present study, the constant-coefficient SGS-flux models of the *a priori* investigation are tested *a posteriori* in LES devoid of, or including, the SGS p-correction term. A new p-correction model, different from that of the *a priori* study, is used, and the results of the two p-correction models are compared. The results reveal that the former is less computationally intensive and more accurate than the latter in reproducing global and structural features of the flow. The constant-coefficient SGS-flux models encompass the Smagorinsky (SMC) model, in conjunction with the Yoshizawa (YO) model for the trace, the gradient (GRC) model and the scale similarity (SSC) models, all exercised with the *a priori* study constant-coefficient values calibrated at the transitional state. Further, dynamic SGS-flux model LESs are performed with the p correction included in all cases. The dynamic models are the Smagorinsky (SMD) model, in conjunction with the YO model, the gradient (GRD) model and 'mixed' models using SMD in combination with GRC or SSC utilized with their theoretical coefficient values. The LES comparison is performed with the filtered-and-coarsened DNS (FC-DNS) which represents an ideal LES solution. The constant-coefficient models including the p correction (SMCP, GRCP and SSCP)

† Email address for correspondence: josette.bellan@jpl.nasa.gov

are substantially superior to those devoid of it; the SSCP model produces the best agreement with the FC-DNS template. For duplicating the local flow structure, the predictive superiority of the dynamic mixed models is demonstrated over the SMD model; however, even better predictions in capturing vortical features are obtained with the GRD model. The GRD predictions improve when LES is initiated at a time past the initial range in which the p-correction term rivals in magnitude the leading-order term in the momentum equation. Finally, the ability of the LES to predict the FC-DNS irreversible entropy production is assessed. It is shown that the SSCP model is the best at recovering the domain-averaged irreversible entropy production. The sensitivity of the predictions to the initial conditions and grid size is also investigated.

1. Introduction

Counterflow motion of different species and species mixing at pressures initially higher than the critical pressure p_c of either fluid has peculiarities not encountered in atmospheric-pressure mixing. Specifically, transcritical-condition experimental observations using jets of various chemical species have identified structures termed 'fingers', or 'comb-like', extending from one of the streams; these structures have an increasingly gaseous appearance with increasing pressure p (Mayer *et al.* 1996, 1998; Chehroudi, Talley & Coy 1999; Oschwald & Schik 1999; Oschwald *et al.* 1999; Segal & Polikhov 2008). All these experiments were performed in the Reynolds number Re regime $O(10^4)$ to $O(10^5)$. No three-dimensional simulations currently exist that can recover the distinctive features of these $p \geqslant p_c$ flows in this Re number regime. This is because of the following reasons: (i) Reynolds-averaged Navier–Stokes simulations are completely inadequate for reproducing the time-dependent strong inhomogeneities observed in these flows. (ii) Direct numerical simulation (DNS) is not routinely feasible for such large Reynolds numbers because of its high computational expense. (iii) Large eddy simulation (LES) is a promising methodology for supercritical-p flows, but so far it has been utilized for $p \geqslant p_c$ flows with models developed for incompressible or atmospheric-p compressible situations (Oefelein & Yang 1998; Zong *et al.* 2004; Oefelein 2005) in which the flow peculiarities discussed above do not exist. Extending current LES models to $p \geqslant p_c$ flows is a necessity if one wishes to simulate gas turbine, diesel or liquid rocket engines in which mixing of species – a precursor to ignition and combustion – occurs at $p \geqslant p_c$ (for mixtures, p_c and the critical temperature T_c depend on the composition (Hirshfelder, Curtis & Bird 1964; Prausnitz, Lichtenthaler & de Azevedo 1986)).

Although DNS is not suitable for practical applications at fully turbulent Re values, it may provide information leading to a thorough understanding of the flow at transitional Re values, thus enabling LES model development. Such DNSs were performed for a temporal mixing layer by Miller, Harstad & Bellan (2001) and Okong'o & Bellan (2002*b*, 2003) using real-gas equations of state (EOSs) for non-ideal mixtures in conjunction with realistic transport properties and thermal diffusion (Soret and Dufour) effects. The results showed that one of the most prominent aspects of $p \geqslant p_c$ flows is the existence of regions of high density-gradient magnitude (HDGM), akin to those seen in the experiments. These HDGM regions were found in both pre-transitional (Miller *et al.* 2001) and transitional (Okong'o & Bellan 2002*b*; Okong'o, Harstad & Bellan 2002) temporal mixing layers and were shown to arise from the combined effect of the distortion of the initial density boundary and of

mixing (Okong'o & Bellan 2002*b*, 2004*b*). It is this filamentary morphology that we call fluid disintegration. Scrutiny of the HDGM composition showed that the HDGM fluid is a mixture of the heavy and light fluids; this situation is very different from that under atmospheric p, where the equivalent of the HDGM regions contains exclusively the heavy fluid, as during atomization.

Further, in an *a priori* analysis of the DNS database (Selle *et al.* 2007), it was found that the utilization of a real-gas EOS (Harstad & Bellan 2000; Okong'o & Bellan 2002*b*) results in the strictly atmospheric-p LES equations being no longer valid, as new significant terms arise from the filtering of the conservation equations. These terms are directly associated with the HDGM regions observed in both simulations and experiments, meaning that the validity of the novel terms extends to Re values higher than those of the transitional databases. The new terms originated from subgrid-scale (SGS) effects and thus required modelling, being conceptually but not mathematically similar to the well-known SGS fluxes. We call these new SGS models 'corrections' because they stemmed from the usual 'LES assumptions' – that the difference between a filtered quantity and the same quantity computed from the filtered flow field is negligible with respect to other terms in the equation – not being satisfied. Two such terms were identified – for the p gradient and the divergence of the heat flux. The p correction was shown to be necessary for the heptane–nitrogen (HN, C_7H_{16}–N_2) system which exhibited strong departures from perfect gas and species ideality, whereas the heat-flux correction term for this species system was negligible. The required heat-flux correction was substantial for the oxygen–hydrogen (OH, O_2–H_2) system, but the p-correction term was negligible; for this species system, the departures from perfect gas and mixture non-ideality are negligible. That a correction is necessary even for small departures from perfect gas and mixture ideality can be understood given the strong nonlinearity of the real-gas EOS, meaning that even slight real-gas or non-ideal mixture behaviour may impart considerable departures from the atmospheric-p LES equations; this is the nature of nonlinearity. For the oxygen–helium (OHe, O_2–He) system, which has modest departures from perfect gas and small departures from mixture non-ideality, the situation was intermediate between the HN and OH systems. Both p-correction and heat-flux correction models were based on Taylor expansion concepts (Selle *et al.* 2007). In the *a priori* analysis, SGS-flux models were also evaluated for the typical SGS fluxes (stresses, heat and species mass). The SGS-flux models evaluated were the Smagorinsky (SM) model (Smagorinksy 1963, 1993), the scale-similarity (SS) model (Bardina, Ferziger & Reynolds 1980) and the gradient (GR) model (Clark, Ferziger & Reynolds 1979). It was concluded that the SM model is inadequate to represent the SGS fluxes, whereas both the SS and the GR model captured the functional form of the SGS fluxes. The poor performance of the SM model was observed despite it being used in conjunction with the well-performing Yoshizawa (YO; Yoshizawa 1986) model for the SGS-stress trace.

Whereas the *a priori* analysis is only concerned with the behaviour of the small turbulent scales, what ultimately matters in LES is the ability of the model to reproduce the interaction among all scales. This interaction is here investigated in an *a posteriori* study in which the *a priori* developed models, as well as other models, are tested in LES, and the results are compared with the DNS database for the HN system (the OH system is relegated to a future study). However, an unprocessed DNS database is not the proper template for comparison with LES. The proper template is the filtered-and-coarsened (FC) DNS: filtered to remove the small scales that are not computed in LES and coarsened to reduce the number of nodes from DNS to those of LES. Thus, the FC-DNS field can be considered as a sample of the DNS

field and a generally ideal, unachievable, LES template. Following the presentation in § 2 of the LES governing equations, the databases are summarized in § 3. The LES initial and boundary conditions are presented in § 4, and the numerical methodology is described in § 5. In § 6, we first address the effectiveness of a p-correction model by comparing two sets of LES that are identical in all respects, except that one set excludes and the other includes the p correction. The p-correction model is in the same spirit but different from that tested *a priori* (Selle *et al.* 2007), and thus its utilization can be considered as a general assessment of the p-correction concept. Having established the necessity of the p correction, the attention is turned to dynamic-coefficient SGS-flux models combined with a p-correction model; we first examine there the influence of the type of p-correction model, after which we compare dynamic-coefficient LESs that use the same p-correction model. Completing the physical picture, the replication in LES of the irreversible entropy production, which is the dissipation (not to be confused with the turbulent kinetic energy, or TKE, dissipation), is addressed. Considerations on initial conditions (ICs) are made in Appendix A, and an inquiry on grid size is presented in Appendix B. All above evaluations are performed using one realization of the DNS database. To assess the general validity of the results, further evaluations are performed for other realizations in the HN database, and for brevity, only some of the pertinent results are presented in Appendix C. Conclusions and a short discussion of future studies are offered in § 7.

2. LES governing equations

The LES equations were derived by Selle *et al.* (2007) from the conservation equations by spatial filtering. The filtering operation is defined as

$$\overline{\psi}(\boldsymbol{x}) = \int_V \psi(\boldsymbol{y}) G(\boldsymbol{x}-\boldsymbol{y})\,\mathrm{d}\boldsymbol{y}, \tag{2.1}$$

where G is the filter function and V is the filtering volume; G has the property that for a spatially invariant function, the filtered function is identical to the unfiltered one. For compressible flows, Favre filtering is used, defined as $\tilde{\psi} = \overline{\rho\psi}/\bar{\rho}$, where ρ is the density. The variance of two quantities φ and θ is defined as $\vartheta(\overline{\varphi},\overline{\theta}) = \overline{\varphi\theta} - \overline{\varphi}\,\overline{\theta}$ or $\vartheta(\widetilde{\varphi},\widetilde{\theta}) = \widetilde{\varphi\theta} - \widetilde{\varphi}\widetilde{\theta}$, depending on the filtering. The governing equations are written for the conservative variables $\phi = \{\rho, \rho u_i, \rho e_t, \rho Y_\alpha\}$ rather than the primitive variables $\psi(\phi) = \{u_i, p, X_\alpha, T\}$, where u_i is the velocity component in the x_i-direction spatial coordinate, e_t is the total energy, T is the temperature, and Y_α and X_α are the mass fraction and mole fraction of species α.

2.1. *LES differential equations*

The LES differential equations, obtained under the assumption that filtering and differentiation commute (the top-hat filter is used here for which the operations commute except near boundaries), are for the HN mixture (Selle *et al.* 2007):

$$\frac{\partial\bar{\rho}}{\partial t} + \frac{\partial\bar{\rho}\tilde{u}_j}{\partial x_j} = 0, \tag{2.2}$$

$$\frac{\partial\bar{\rho}\tilde{u}_i}{\partial t} + \frac{\partial\bar{\rho}\tilde{u}_i\tilde{u}_j}{\partial x_j} = -\frac{\partial p\left(\overline{\phi}\right)}{\partial x_i} + \frac{\partial\sigma_{ij}\left(\overline{\phi}\right)}{\partial x_j} - \frac{\partial}{\partial x_j}\left(\bar{\rho}\tau_{ij}\right) - \frac{\partial}{\partial x_i}\left[\overline{p(\phi)} - p\left(\overline{\phi}\right)\right], \tag{2.3}$$

$$\frac{\partial \bar{\rho}\tilde{e}_t}{\partial t} + \frac{\partial \bar{\rho}\tilde{e}_t\tilde{u}_j}{\partial x_j} = -\frac{\partial p\left(\overline{\phi}\right)\tilde{u}_j}{\partial x_j} - \frac{\partial q_{IKj}\left(\overline{\phi}\right)}{\partial x_j} + \frac{\partial \sigma_{ij}\left(\overline{\phi}\right)\tilde{u}_i}{\partial x_j} - \frac{\partial}{\partial x_j}\left(\bar{\rho}\zeta_j\right) - \frac{\partial\left(\bar{\rho}\tau_{ij}\widetilde{u}_i\right)}{\partial x_j}, \tag{2.4}$$

$$\frac{\partial \bar{\rho}\tilde{Y}_\alpha}{\partial t} + \frac{\partial \bar{\rho}\tilde{Y}_\alpha\tilde{u}_j}{\partial x_j} = -\frac{\partial j_{\alpha j}\left(\overline{\phi}\right)}{\partial x_j} - \frac{\partial}{\partial x_j}(\bar{\rho}\eta_{\alpha j}), \tag{2.5}$$

where the SGS fluxes are

$$\tau_{ij} = \vartheta(\widetilde{u}_i, \widetilde{u}_j), \quad \zeta_j = \vartheta(\tilde{h}, \tilde{u}_j), \quad \eta_{\alpha j} = \vartheta(\widetilde{Y}_\alpha, \widetilde{u}_j) \text{ with } \sum_{\alpha=1}^{N}\eta_{\alpha j} = 0, \tag{2.6}$$

and the additional SGS term modelled *a priori* by Selle *et al.* (2007) is $\nabla[\overline{p(\phi)} - p(\overline{\phi})]$. In (2.2)–(2.5), t is the time; σ is the viscous stress tensor; $\boldsymbol{q}_{IK}$ is the Irwing–Kirkwood (denoted by the subscript IK) heat flux (Sarman & Evans 1992); $e = e_t - e_K$ is the internal energy; $e_K = u_i u_i/2$ is the kinetic energy; N is the number of species; and $\boldsymbol{j}_\alpha$ is the species-mass flux of species α. Furthermore,

$$\sum_{\alpha=1}^{N} Y_\alpha = 1, \quad \sum_{\alpha=1}^{N} j_{\alpha j} = 0. \tag{2.7}$$

Here, the Einstein summation is used for roman indices (i, j, k) but not for Greek indices (α, β). The thermodynamic variables are functions of the LES flow field $\overline{\phi}$:

$$e = e\left(\overline{\phi}\right), \quad p = p\left(\overline{\phi}\right), \quad Y = Y\left(\overline{\phi}\right), \quad T = T\left(\overline{\phi}\right), \quad h = h\left(\overline{\phi}\right), \tag{2.8}$$

where p, T and the enthalpy $h = e + p/\rho$ are computed from the EOS. Likewise, the fluxes are functions of $\overline{\phi}$:

$$\sigma_{ij} = \sigma_{ij}\left(\overline{\phi}\right), \quad j_{\alpha j} = j_{\alpha j}\left(\overline{\phi}\right), \quad q_{IKj} = q_{IKj}\left(\overline{\phi}\right). \tag{2.9}$$

For a Newtonian fluid,

$$\sigma_{ij} = \mu\left(\frac{\partial u_i}{\partial x_j} + \frac{\partial u_j}{\partial x_i} - \frac{2}{3}\frac{\partial u_k}{\partial x_k}\delta_{ij}\right), \quad S_{ij} = \frac{1}{2}\left(\frac{\partial u_i}{\partial x_j} + \frac{\partial u_j}{\partial x_i}\right), \tag{2.10}$$

where μ is the viscosity and S_{ij} is the rate-of-strain tensor.

The species-mass and heat fluxes originate in the fluctuation–dissipation theory (see Keizer 1987), which is consistent with non-equilibrium thermodynamics, converges to kinetic theory in the low-p limit and relates fluxes and forces from first principles. For a binary-species system (light species 1, heavy species 2), the species-mass and heat fluxes, including the Soret and Dufour effects (Harstad & Bellan 2000), are

$$\boldsymbol{j}_2(\overline{\psi}) = B_Y(\overline{\psi})\nabla Y_2\left(\overline{\phi}\right) + B_T(\overline{\psi})\nabla T\left(\overline{\phi}\right) + B_P(\overline{\psi})\nabla p\left(\overline{\phi}\right), \tag{2.11}$$

$$\boldsymbol{q}_{IK}(\overline{\psi}) = C_Y(\overline{\psi})\nabla Y_2\left(\overline{\phi}\right) + C_T(\overline{\psi})\nabla T\left(\overline{\phi}\right) + C_P(\overline{\psi})\nabla p\left(\overline{\phi}\right), \tag{2.12}$$

where $\overline{\psi} \equiv \psi(\overline{\phi})$ and functionally

$$B_Y \equiv -\rho D\alpha_D, \qquad C_Y \equiv -\rho D\alpha_D\alpha_{IK}R_u T\frac{m}{m_1 m_2}, \tag{2.13}$$

$$B_T \equiv -\alpha_{BK}Y_1Y_2\frac{\rho D}{T}, \qquad C_T \equiv -\lambda - \rho D\alpha_{IK}\alpha_{BK}R_u\frac{m}{m_1 m_2}Y_1Y_2, \tag{2.14}$$

$$B_P \equiv -\rho D\frac{Y_1Y_2}{R_u T}\frac{m_2 m_1}{m}\Lambda, \qquad C_P \equiv -\rho D\alpha_{IK}\Lambda Y_1Y_2. \tag{2.15}$$

Species	m (g mol^{-1})	T_c (K)	p_c(MPa)
N_2	28.013	126.3	3.399
C_7H_{16}	100.205	540.2	2.74

TABLE 1. Pure species properties.

In (2.13)–(2.15),

$$\alpha_{BK} = \alpha_{IK} - \alpha_h, \quad \alpha_h = \frac{1}{R_u T}\frac{m_2 m_1}{m}\Theta, \tag{2.16}$$

$$\Lambda \equiv \left(\frac{1}{m_2}\frac{\partial v}{\partial X_2} - \frac{1}{m_1}\frac{\partial v}{\partial X_1}\right), \quad \Theta \equiv \left(\frac{1}{m_2}\frac{\partial (mh)}{\partial X_2} - \frac{1}{m_1}\frac{\partial (mh)}{\partial X_1}\right), \tag{2.17}$$

$$\alpha_D \equiv 1 + X_\alpha \frac{\partial \ln \gamma_\alpha}{\partial X_\beta}, \tag{2.18}$$

where λ is the thermal conductivity with $\lim_{p\to 0}\lambda = \lambda_{KT}$ as discussed in Harstad & Bellan (2000); the subscript KT denotes the kinetic theory; R_u is the universal gas constant; m is the mixture molar mass; and v is the molar volume with $v = m/\rho$. For species α, m_α is the molar mass, $X_\alpha = mY_\alpha/m_\alpha$ and γ_α is the fugacity. Furthermore, α_{IK} is the IK form of the thermal diffusion factor; α_{BK} is the Bearman–Kirkwood (denoted by the subscript BK) form of the thermal diffusion factor; D is the binary diffusion coefficient; and α_D is the mass diffusion factor.

The models for the unclosed terms in (2.2)–(2.5), namely τ_{ij}, ζ_j, $\eta_{\alpha j}$ and $\nabla[\overline{p(\phi)} - p(\overline{\phi})]$, for the HN mixture are described in § 2.4.1.

2.2. *Equation of state*

The pressure is calculated from the well-known Peng–Robinson (PR) EOS, given T and the PR molar volume (v_{PR}), as

$$p = \frac{R_u T}{(v_{PR} - b_m)} - \frac{a_m}{\left(v_{PR}^2 + 2b_m v_{PR} - b_m^2\right)}, \tag{2.19}$$

where a_m and b_m are functions of T and X_α, the mathematical forms of which are given in detail in Miller *et al.* (2001) and Okong'o *et al.* (2002). At high p, the v_{PR} value may differ significantly from that of v (Prausnitz *et al.* 1986), but this difference is negligible for the HN system (Harstad, Miller & Bellan 1997). All thermodynamic quantities, including α_D, h, $C_p = (\partial h/\partial T)_{p,X}$ and the speed of sound (a_s), are calculated from the EOS using standard thermodynamic relations (Miller *et al.* 2001; Okong'o & Bellan 2002*b*; Okong'o *et al.* 2002). The implementation of the EOS to calculate p and T from ρ, e and Y_α uses an energy fit (Okong'o & Bellan 2002*b*) for the HN mixture. The pure species properties are listed in table 1.

2.3. *Transport coefficients*

The viscosity, the Schmidt number ($Sc = \mu/(\rho\alpha_D D)$) and the Prandtl number ($Pr = \mu C_p/(m\lambda)$) were calculated from high-pressure single-species transport properties using mixing rules, as in Harstad & Bellan (1998). The calculated values were correlated, as summarized in table 2, and these correlations are then used to compute the transport properties μ, D and λ. The relationship between α_{BK} and α_{IK} stated in (2.16) means that either one can be specified, and the other can then be calculated.

Transport property	Model
$\mu = \mu_R (T/T_R)^n$	$n = 0.7$
$Sc \equiv \mu/(\rho \alpha_D D)$	$1.5 - Y_h$
$Pr \equiv \mu C_p/(m\lambda)$	$0.5Sc/\exp(-1.5Y_h)$
α_{IK}	0.1

TABLE 2. Transport properties for binary mixtures; $T_R = (T_1 + T_2)/2$, T in Kelvin; α_{IK} is from Harstad & Bellan (2000). The functional fits are valid over the T range of 500–1100 K and the p range of 40–80 atm.

2.4. *SGS models*

2.4.1. *SGS-flux models*

Three categories of models are here employed for SGS fluxes (τ_{ij}, $\eta_{\alpha j}$, ζ_j), namely constant-coefficient models, dynamic models and dynamic mixed models.

The constant-coefficient SGS models considered are the Smagorinsky (SMC; Smagorinksy 1963, 1993), the gradient (GRC; Clark *et al.* 1979) and the scale-similarity models (SSC; Bardina *et al.* 1980).

The SMC model is based on the gradient-diffusion (eddy-viscosity) concept. As such it does not lend itself to computing variances in general. The SGS fluxes in (2.6) are

$$\vartheta_{SM}(\widetilde{\psi}_m, \tilde{u}_j) = -C_{SM}\bar{\Delta}^2 S\left(\bar{\phi}\right)\frac{1}{2}\frac{\partial \widetilde{\psi}_m}{\partial x_j}, \qquad \psi_m \neq u_j, \tag{2.20}$$

with τ_{ij} modelled in trace-free form as

$$\tau_{ij} - \frac{1}{3}\tau_{kk}\delta_{ij} = -C_{SM}\bar{\Delta}^2 S\left(\bar{\phi}\right)\left[S_{ij}\left(\bar{\phi}\right) - \frac{1}{3}S_{kk}\left(\bar{\phi}\right)\delta_{ij}\right], \tag{2.21}$$

where $S^2(\phi) = S_{ij}(\phi)S_{ij}(\phi)$. The YO (Yoshizawa 1986) model for τ_{kk} is

$$\tau_{kk} = C_{YO}\bar{\Delta}^2 S^2\left(\bar{\phi}\right). \tag{2.22}$$

The GRC model, derived from a Taylor series expansion (Okong'o & Bellan 2004*a*), is

$$\vartheta_{GR}(\widetilde{\psi}_m, \widetilde{\psi}_n) = C_{GR}\bar{\Delta}^2\frac{\partial \tilde{\psi}_m}{\partial x_k}\frac{\partial \tilde{\psi}_n}{\partial x_k}. \tag{2.23}$$

(Note that $\vartheta(\tilde{u}_1, \tilde{u}_1) = \tau_{11}$, $\vartheta(\tilde{u}_2, \tilde{u}_2) = \tau_{22}$, $\vartheta(\tilde{u}_3, \tilde{u}_3) = \tau_{33}$.) Theoretically, C_{GR} is proportional to the moments of inertia of the filtering volume; for a cubic top-hat filter $C_{GR} = 1/12$ (Okong'o & Bellan 2004*a*).

The SSC model, which postulates similarity between the SGS and the small resolved scale, is (Bardina *et al.* 1980)

$$\vartheta_{SS}(\widetilde{\psi}_m, \widetilde{\psi}_n) = C_{SS}\left(\widehat{\widetilde{\psi}_m\widetilde{\psi}_n} - \widehat{\widetilde{\psi}}_m\widehat{\widetilde{\psi}}_n\right), \tag{2.24}$$

where the overhat ($\widehat{\ }$) denotes (unweighted) filtering at the test-filter level $\hat{\Delta}$. The test-filter width considered is $\hat{\Delta}/\bar{\Delta} = 2$, as is generally recommended. While scale similarity would imply that $C_{SS} = 1$, the actual value is filter-width dependent (Clark *et al.* 1979; Liu, Meneveau & Katz 1994; Pruett, Sochacki & Adams 2001; Okong'o & Bellan 2004*a*).

For transient flows with strong inhomogeneities, constant-coefficient models may not be accurate enough. An increase in accuracy may be expected from a solution in which the coefficients are computed using the LES solution through dynamic modelling. The premise of dynamic modelling is that a scale similarity exists, and thus the SGS behaviour may be deduced from that of the small resolved scales. A test filter is introduced, $\hat{\Delta}$, such that $\hat{\Delta} > \bar{\Delta}$, and through the action of double filtering, $\widehat{\hat{\Delta}}$, a field with scales larger than the resolved field is generated. Here $\widehat{\hat{\Delta}}$ is the effective filter width, not actually used for filtering, that corresponds to filtering at $\bar{\Delta}$ followed by filtering at $\hat{\Delta}$ and the value of which depends on the filter type. For the top-hat filter used here for both the grid and the test filter, $\widehat{\hat{\Delta}}$ is optimally approximated by $\widehat{\hat{\Delta}}^2 = \bar{\Delta}^2 + \hat{\Delta}^2$ (Vreman, Geurts & Kuerten 1997). The essence of dynamic modelling is to relate the grid-level SGS flux and the test-level SGS flux to the test-level resolved flux. For any quantity φ, such as $\tilde{h}$, $\widetilde{Y_\alpha}$ or $\tilde{u}_i$, the grid-level and test-level SGS fluxes associated with the velocity $\tilde{u}_j$ are denoted as $\vartheta_j(\varphi)$ and $\mathscr{T}_j(\varphi)$, respectively, and are defined as

$$\vartheta_j(\varphi) = \widetilde{\varphi u_j} - \tilde{\varphi}\tilde{u}_j, \tag{2.25}$$

$$\mathscr{T}_j(\varphi) = \vartheta_j(\widehat{\varphi}) = \widehat{\widetilde{\varphi u_j}} - \hat{\tilde{\varphi}}\hat{\tilde{u}}_j, \tag{2.26}$$

where $\vartheta_j(u_i) = \tau_{ij}$, $\vartheta_j(Y_V) = \eta_j$ and $\vartheta_j(h) = \zeta_j$. The test-level resolved flux L_j is computed through the Germano identity (Germano *et al.* 1991). For compressible flows, L_j takes the form (Moin *et al.* 1991)

$$L_j(\varphi) \equiv \hat{\bar{\rho}}\mathscr{T}_j - \widehat{\bar{\rho}\vartheta_j} = \widehat{\bar{\rho}\tilde{\varphi}\tilde{u}_j} - \frac{\widehat{\bar{\rho}\tilde{\varphi}}\,\widehat{\bar{\rho}\tilde{u}}_j}{\widehat{\bar{\rho}}}, \tag{2.27}$$

where $\widehat{\widetilde{\psi}} = \widehat{\bar{\rho}\psi}/\widehat{\bar{\rho}}$. In the above equation, $\vartheta_j(\varphi)$ can be modelled using the generic model coefficient $C(\varphi)$ as

$$\vartheta_j(\varphi) = C(\varphi)\mu_j\big(\varphi, \bar{\Delta}\big), \tag{2.28}$$

where $\mu_j(\varphi, \bar{\Delta})$ is associated with the filter width $\bar{\Delta}$ and the velocity $\tilde{u}_j$. In a similar fashion, $\mathscr{T}_j$ can be modelled as $\mu_j(\widehat{\varphi}, \widehat{\hat{\Delta}})$, associated with $\widehat{\hat{\Delta}}$ and the velocity $\widehat{\tilde{u}}_j$. If $C(\varphi)$ is assumed to be constant within the test filter, then the left-hand side of (2.27) can be calculated in terms of $C(\varphi)$ as

$$L_j(\varphi) = C(\varphi)M_j(\varphi) = C(\varphi)(\hat{\bar{\rho}}\mu_j(\widehat{\varphi}) - \widehat{\bar{\rho}\mu_j(\varphi)}). \tag{2.29}$$

Here, the SGS-flux model, μ_j, can be chosen to be any of the mathematical forms given in (2.20)–(2.24), excluding the model coefficient.

Despite the observation in the *a priori* study (Selle *et al.* 2007) that the SSC and GRC models have much better correlations with the SGS fluxes than does the SMC model, we still investigate the predictive abilities of the SM model not only in its constant-coefficient or dynamic form but also as the underlying model for 'mixed' models (Speziale *et al.* 1988; Zang, Street & Koseff 1993; Vreman, Geurts & Kuerten 1996*b*). Typically, in mixed models, the SM model is used with the addition of similarity-based models. The popular belief is that while the SM model provides the necessary dissipation to keep the simulation numerically stable, the similarity-based models contribute the structural details lacking in the SM model. However, this is not the reason that mixed models are used here, as explained in § 6.2, because our computations have no numerical stability issues.

In the present dynamic mixed-model calculations, the SM model is used in combination with either the gradient model (MGRD) or the scale-similarity model (MSSD). The dynamic mixed model follows the approach of Vreman *et al.* (1997): the coefficient of the SM model is dynamically calculated, and those of the similarity-based models are kept constant at their theoretical value.

For dynamic mixed models, (2.29) becomes

$$L_j(\varphi) = H_j(\varphi) + C(\varphi)M_j(\varphi), \tag{2.30}$$

with $H_j(\varphi) = (\hat{\bar{\rho}}\hat{\vartheta}_j(\hat{\varphi}) - \widehat{\bar{\rho}\vartheta_j(\varphi)})$, and ϑ_j is computed using the theoretical values $C_{GR} = 1/12$ and $C_{SS} = 1$ for the GR and SS models, respectively (Okong'o & Bellan 2004*a*). Following Lilly (1992), we use a least squares method to minimize the error in computing the coefficient from an overdetermined equation set, which yields the coefficients

$$C_H(\varphi) = \frac{\langle (L_j(\varphi) - H_j(\varphi))M_j(\varphi)\rangle}{\langle M_j(\varphi)\, M_j(\varphi)\rangle} \quad \text{or} \quad C_D(\varphi) = \frac{\langle\langle (L_j(\varphi) - H_j(\varphi))M_j(\varphi)\rangle\rangle}{\langle\langle M_j(\varphi)\, M_j(\varphi)\rangle\rangle}, \tag{2.31}$$

where, for the present mixing-layer configuration, $\langle\rangle$ denotes averaging over homogeneous (x_1, x_3) planes, while $\langle\langle\rangle\rangle$ denotes averaging over the entire domain. For the SM model, the summation over repeated indices in (2.31) is over three quantities for the SGS-stress diagonal terms and over three quantities for the SGS-stress off-diagonal terms. Unlike for the SM model, the summation for the GR model is over six quantities for the SGS-stress terms. For all dynamic models, both ζ_j and η_j are found by summation over the three components. (The use of dimensional variables in the present formulation necessitates the separate computation of the coefficient for each type of SGS flux.) The simulations are performed with a multi-coefficient formulation, where there is a different coefficient for each type of flux according to

$$C(\tau_{ij}) = C_\tau, \quad C(\zeta_j) = C_\zeta, \quad C(\eta_j) = C_\eta. \tag{2.32}$$

For the SM-based models, there are two different coefficients associated with the anisotropic and the isotropic part of the stress tensor as

$$C(\tau_{ij,i=j}) = C_{\tau d},\ C(\tau_{ij,i\neq j}) = C_{\tau x}. \tag{2.33}$$

The dynamic coefficient values replacing those of the constant coefficients are computed as follows:

(*a*) For the dynamic SM (SMD) model, μ_j is computed from (2.20)–(2.22), and $H_j = 0$.

(*b*) For the dynamic mixed GR (MGRD) model, μ_j is computed from (2.20)–(2.22), and ϑ_j in H_j is computed from (2.23) using $C_{GR} = 1/12$.

(*c*) For the dynamic mixed SS (MSSD) model, μ_j is computed from (2.20)–(2.22), and ϑ_j in H_j is computed from (2.24) using $C_{SS} = 1$.

(*d*) For the dynamic GR (GRD) model, μ_j is computed from (2.23), and $H_j = 0$.

2.4.2. *Pressure correction*

To model $\nabla[\overline{p(\phi)} - p(\overline{\phi})]$, Selle *et al.* (2007) have expanded the EOS (2.19) in a Taylor series around the reference state $\overline{\phi}$, obtaining

$$\overline{p(\phi)} = \overline{p(\overline{\phi})} + \overline{\frac{\partial p}{\partial \phi_m}\bigg|_{\phi=\overline{\phi}} (\phi_m - \overline{\phi_m})} + \overline{\frac{1}{2}\frac{\partial^2 p}{\partial\phi_m\partial\phi_n}\bigg|_{\phi=\overline{\phi}} (\phi_m - \overline{\phi_m})(\phi_n - \overline{\phi_n})} + \text{h.o.t.} \tag{2.34}$$

The developed model was under the verified assumption that $(\phi - \overline{\phi})$ is small (at $\overline{\Delta} = 4\Delta x_{DNS}$ and $\overline{\Delta} = 8\Delta x_{DNS}$) and under the non-rigorous assumptions that

$$\overline{p\,(\overline{\phi})} = p\,(\overline{\phi}), \tag{2.35}$$

that $(\partial p/\partial \phi_m)_{\phi=\overline{\phi}}$ and $(\partial^2 p/(\partial \phi_m \partial \phi_n))_{\phi=\overline{\phi}}$ can be removed from the filtering operation and that the filter is a projection which implies that $(\overline{\phi_m} - \overline{\overline{\phi_m}}) = 0$, all of which led to

$$\overline{p\,(\phi)} = p\,(\overline{\phi}) + \delta, \quad \delta = \frac{1}{2}\,\frac{\partial^2 p}{\partial \phi_m \partial \phi_n}\bigg|_{\phi=\overline{\phi}} \left(\overline{\phi_m \phi_n} - \overline{\phi_m}\;\overline{\phi_n}\right) = \frac{1}{2}\,\frac{\partial^2 p}{\partial \phi_m \partial \phi_n}\bigg|_{\phi=\overline{\phi}} \vartheta(\overline{\phi_m}, \overline{\phi_n}), \tag{2.36}$$

where m and n index the components of vectors ϕ and ψ and δ is the second-order approximation in the LES assumption for the pressure. Extensive and tedious mathematics permitted the computation of $(\partial^2 p/(\partial \phi_m \partial \phi_n))_{\phi=\overline{\phi}}$ from the knowledge of $(\partial^2 p/(\partial \psi'_m \partial \psi'_n))_{\psi'=\overline{\psi'}}$, where $\psi'(\phi) = \{u_i, v, X_\alpha, T\}$, through the PR EOS. The quantities $\vartheta(\overline{\phi_m}, \overline{\phi_n})$ in (2.36) are not inherent SGS models, as they do not appear directly as a result of equation filtering but rather as the result of the chosen p-correction model. Consistent with other variance models, $\vartheta(\overline{\phi_m}, \overline{\phi_n})$ were modelled using one of the SGS-flux models described in § 2.4.1. The results showed excellent success at a filter size $\overline{\Delta} = 4\Delta x_{DNS}$, where the DNS grid spacing was uniform with $\Delta x_1 \simeq \Delta x_2 \simeq \Delta x_3$ and $\Delta x_{DNS} = \max\{\Delta x_i\}$; however, a model deterioration was evident at $\overline{\Delta} = 8\Delta x_{DNS}$. Because the assumption that '$(\phi - \overline{\phi})$ is small' is justified even at $\overline{\Delta} = 8\Delta x_{DNS}$, this deterioration is attributed to two consequences of the assumption that the filter is a projection: (i) the nulling of the first-order term in the Taylor expansion and (ii) the approximation of the differences in the second-order term using SGS-flux models for the variances.

The present approach for modelling $[\overline{p(\phi)} - p(\overline{\phi})]$ is different from that developed by Selle *et al.* (2007) because the wish is to improve the chances of success at higher filter size than $\overline{\Delta} = 4\Delta x_{DNS}$. Indeed, for LES to be computationally beneficial with respect to DNS, the minimum $\Delta x_{LES} = 2\Delta x_{DNS}$ (a factor of eight increase in the computational volume). Since it has been recommended that a minimum $\overline{\Delta} = 2\Delta x_{LES} = 4\Delta x_{DNS}$ should be chosen in order to ensure that the SGS term is larger than numerical errors (Ghosal 1996; Chow & Moin 2003), this implies that $\overline{\Delta} = 4\Delta x_{DNS}$ is the minimum acceptable filter value. Realistically, it is more desirable to have $\Delta x_{LES} = 4\Delta x_{DNS}$, which would mean an increase by a factor of 64 in the computational volume for LES compared with DNS, implying that a more realistic value of the filter size is $\overline{\Delta} = 2\Delta x_{LES} = 8\Delta x_{DNS}$, the value for which the model of Selle *et al.* (2007) for the second-order Taylor expansion term showed deteriorating results. This situation motivated the development of a new p-correction model.

Thus, we no longer assume here that the filter is a projection, although we still assume that $(\partial p/\partial \phi_m)_{\phi=\overline{\phi}}$ can be removed from the filtering operation, being a constant in the filtering volume, as it is evaluated at its centre node. Thus, the model is now

$$\overline{p\,(\phi)} = \overline{p\,(\overline{\phi})} + \frac{\partial p}{\partial \phi_m}\bigg|_{\phi=\overline{\phi}} \left(\overline{\phi_m} - \overline{\overline{\phi_m}}\right). \tag{2.37}$$

The quantity $\overline{\phi_m}$ is the LES solution and $\overline{\overline{\phi_m}}$ is computed by filtering the LES solution. The idea behind using the first-order Taylor series term is that it inherently is a more accurate approximation of $[\overline{p(\phi)} - p(\overline{\phi})]$ than the second-order term only. Thus, we now rely uniquely on the first-order term of the Taylor expansion, as the second-order

term is not easily modelled without the assumption of the filter being a projection, which nulls the first-order term. Results using the first-order p correction (FOC) for the LES described in § 6 are compared in § 6.2.1 with results using the second-order p correction (SOC) at same ICs. Otherwise, when a p-correction model is used, all LESs in § 6 employ the FOC $[\overline{p(\phi)} - p(\overline{\phi})]$ model.

The model of (2.37) was implemented in (2.3) by computing

$$\nabla(p(\overline{\phi})) + \nabla(\overline{p\,(\phi)} - p\,(\overline{\phi})) = \nabla(\overline{p\,(\phi)}) = \nabla\left[\overline{p\,(\overline{\phi})} + \left.\frac{\partial p}{\partial \phi_m}\right|_{\phi=\overline{\phi}} \left(\overline{\phi_m} - \overline{\overline{\phi_m}}\right)\right], \quad (2.38)$$

where $p(\overline{\phi})$ is the p value computed in LES.

3. Description of the DNS database

The DNS database consists of supercritical temporal mixing-layer simulations of a two species ($N = 2$) HN (heptane, subscript h; nitrogen, subscript n) mixture. Because the DNSs described in Okong'o & Bellan (2002*b*) and analysed *a priori* by Selle *et al.* (2007) were performed on a previous computer platform which has now been superseded by a faster supercomputer, the same DNS code used by Okong'o & Bellan (2002*b*) was used to re-create the database on the current supercomputer to enable CPU-time comparisons with the LES. The newly obtained DNS results were carefully compared with the previous ones (Okong'o & Bellan 2002*b*) to ensure agreement within machine accuracy.

A detailed description of the DNS methodology has been given by Miller *et al.* (2001) and Okong'o & Bellan (2002*b*). The DNS differential equations combined with the EOS described in § 2.2, using the transport coefficient models presented in § 2.3, were numerically solved using a fourth-order explicit Runge–Kutta time integration and a sixth-order compact scheme with eighth-order filter for spatial derivatives (Kennedy & Carpenter 1994); the filtering (applied at interior points only) is required to maintain numerical stability for long-time integrations, but since it acts only on the shortest waves that can be resolved on the grid, it does not act as a turbulence model allowing under-resolved computations. The computations were parallelized using three-dimensional domain decomposition and message passing and an efficient parallel tridiagonal solver (Muller & Scheerer 1991).

The configuration is that of a temporally developing mixing layer, as depicted in figure 1, which shows the definition of the streamwise (x_1), cross-stream (x_2) and spanwise (x_3) coordinates. Species 1 and 2 initially reside in the upper and the lower stream, respectively. The layer is not symmetric in extent in the x_2 direction, to accommodate the larger layer growth in the lighter fluid side. The free-stream density (ρ_1 or ρ_2) is calculated for each pure species at its free-stream temperature (T_1 or T_2) and at the initial uniform pressure (p_0). The vorticity thickness is defined as $\delta_\omega(t) = \Delta U_0/(\partial\langle u_1\rangle/\partial x_2)_{max}$, where $\Delta U_0 = U_1 - U_2$ is the velocity difference across the layer; U_1 and U_2 were chosen with the intent of keeping the ultimate vortex stationary in the computational domain (Papamoschou & Roshko 1988; Miller *et al.* 2001); the specification of the convective Mach number (see table 3) $M_{c,0}$ determines ΔU_0. Given the initial streamwise velocity profile u_1 based on U_1 and U_2, $(\partial\langle u_1\rangle/\partial x_2)_{max}$ and hence $\delta_{\omega,0} \equiv \delta_\omega(0)$ are calculated. The initial momentum ratio $|\rho_2 U_2|/|\rho_1 U_1| \sim 5$ and the initial momentum flux ratio $(\rho_2 U_2^2)/(\rho_1 U_1^2) = 2.2$. The specified value of the initial flow Reynolds number $Re_0 = (1/2)(\rho_1 + \rho_2)\Delta U_0 \delta_{\omega,0}/\mu_R$, chosen so as to enable the resolution of all relevant length scales, is then used to calculate μ_R, which scales μ.

Run	Re_0	$\lambda_1/\delta_{\omega,0}$	$L_1 \times L_2 \times L_3$ (m^3)	$N_1 \times N_2 \times N_3$	Δx (10^{-4} m)	$Re_{m,tr}$	t^*_{tr}	CPU (h)
HN500	500	7.29	0.200×0.232×0.120	240×288×144	8.36	1250	155	371
HN600	600	7.29	0.200×0.232×0.120	288×336×176	6.97	1452	135	667
HN800	800	4.57	0.125×0.148×0.075	240×272×144	5.23	1258	100	356

TABLE 3. Listing of the DNS realizations and associated resolution; L_i is the size of the domain in the x_i direction, in metres. For all layers, $L_1=4\lambda_1$, $\delta_{\omega,0}=6.859\times10^{-3}$ m, $F_{2D}=0.1$ and $F_{3D}=0.05$. Moreover, $p_0 = 60$ atm, $T_1 = 1000$ K, $T_2 = 600$ K and $\rho_2/\rho_1 = 12.88$, with $M_{c,0}=0.40$. The subscript tr denotes the transitional time. The CPU time is an estimate, based on an aggregate over parallel processors on an SGI Altix 3000 system and represents the time used to reach the DNS transitional time.

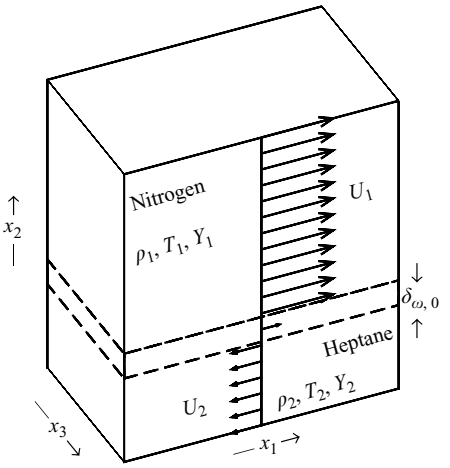

FIGURE 1. The C_7H_{16}–N_2 mixing-layer configuration.

The grid spacing is approximately inversely proportional to Re_0, suggested by the relationship $l/\eta_K \sim Re^{3/4}$ (Tennekes & Lumley 1989), where l is the integral scale and η_K is the Kolmogorov scale.

The simulations are started with error-function profiles for the mean streamwise velocity, mass fraction and temperature, upon which are imposed spanwise and streamwise vorticity perturbations (Moser & Rogers 1991, 1993) of strengths F_{2D} and F_{3D} respectively, whose streamwise (λ_1) and spanwise (λ_3) wavelengths are $\lambda_1=C\delta_{\omega,0}$ and $\lambda_3=0.6\lambda_1$, where $C=7.29$ is the most unstable wavelength for incompressible flow. For the simulations reported here, listed in table 3, another value of C obtained from stability analyses (Okong'o & Bellan 2003) was also used: $C = 4.57$ for the shortest (estimated) unstable wavelength. The grid is chosen for all simulations so as to accommodate four wavelengths in the streamwise and spanwise directions, and the evolution of the layer is meant to encompass roll-up and two pairings of the four initial spanwise vortices into an ultimate vortex.

The boundary conditions are periodic in the x_1 and x_3 directions and of outflow type for real gas in the x_2 direction, as derived by Okong'o & Bellan (2002*a*). The outflow-type conditions are essential to maintain numerical stability, since the initial perturbation causes large p waves that must be allowed out of the domain with minimal reflection.

The database used for the *a priori* analysis is summarized in table 3, including the transitional time $t^*_{tr} = t_{tr}\Delta U_0/\delta_{\omega,0}$ and the value of the momentum-thickness-based Reynolds number $Re_m = Re_0\delta_m/\delta_{\omega,0}$ at transition, where

$$\delta_m = \frac{\displaystyle\int_{x_2,min}^{x_2,max} \left[\langle\rho u_1\rangle_{x_2,max} - \langle\rho u_1\rangle\right]\left[\langle\rho u_1\rangle - \langle\rho u_1\rangle_{x_2,min}\right] \mathrm{d}x_2}{\left(\langle\rho u_1\rangle_{x_2,max} - \langle\rho u_1\rangle_{x_2,min}\right)^2}, \tag{3.1}$$

with $x_{2,max} = L_2/2$, $x_{2,min} = -L_2/2$ (Okong'o & Bellan 2002*b*) and t_{tr} is the time at which the one-dimensional velocity-fluctuation-based energy spectra become smooth, except for the forcing frequency. The goal of the LES is to reproduce the features of the FC-DNS, with special attention to the HDGM regions which populate the entire mixing layer. Their significance has been discussed by Miller *et al.* (2001) and Bellan (2006): the effect of the HDGM regions is to redistribute turbulent energy from the normal direction to the tangential direction, as found in the experiments of Hannoun, Fernando & List (1988) at sharp density boundaries. Unless one can capture this local aspect of the flow, it is very unlikely that mixing and combustion could be faithfully simulated in gas turbine, diesel or liquid rocket engines. For thinner HDGM regions, the corresponding LES may require higher resolution relative to DNS (i.e. less grid coarsening, smaller $\bar{\Delta}/\Delta x_{DNS}$ and $\Delta x_{LES}/\Delta x_{DNS}$) than LES with thicker HDGM regions, since the appropriate Δx_{LES} depends on the gradients of the filtered flow field.

4. LES initial and boundary conditions

In *a posteriori* LES studies, the choice of the ICs is distinct from that for LES of practical flows in which comparison is performed with experimental data. In the present study in which LES will be compared with DNS results, it is natural to think that the simulations should start with the same ICs. However, a function well resolved on a DNS grid cannot be represented with the same accuracy on an LES grid, which is coarser. Additionally, filtering results in loss of information. Since the LES equations are obtained from the original conservation equations through filtering, it is also natural to assume that filtering the DNS ICs should be the first step (e.g. Vreman *et al.* 1997; Geurts & Frohlich 2002; Leboissetier, Okong'o & Bellan 2005), followed by grid coarsening to retain only those nodes that will be used in LES. This is indeed the approach typically followed, and it has been adopted here as well; this is what we call the FC-DNS. Another approach is to compute analytically prescribed ICs on the LES grid, followed by filtering. If so, there are two choices in filtering: one could filter using all DNS points (as in the FC-DNS) or only using the LES grid; we call the latter choice a coarsened-and-filtered (CF) DNS database. Although the same filter is used in both cases, application of the numerical filter over the coarse grid yields slightly different ICs than those over the fine grid; and this small difference affects the solution. It turns out that this CF-DNS choice of ICs yields LES results that are closer to the FC-DNS during the layer development (including transition) than the LES using the FC-DNS ICs is with respect to the FC-DNS during the entire layer evolution. The reason that both solutions are compared with the FC-DNS is that the LES template is the filtered DNS solution, which is unique irrespective of LES considerations (e.g. the LES ICs). The CF-DNS results are presented in Appendix A. An alternate way to conduct LES is to provide ICs at a $t^* > 0$ DNS time station rather than at $t^* = 0$ (e.g. Geurts & Frohlich 2002). The advantage of initiating

LES at a $t^* > 0$ DNS time station is that one may choose t^* to be past all large transients associated with the p evolution from the IC, a choice which dramatically improves the agreement between the LES and the FC-DNS. Two such examples are provided: one for constant-coefficient models in Appendix A (where some *a priori* tabulated results that identify the time station at which the p-correction term begins to no longer rival the leading-order term in the momentum equation are also shown) and another for dynamic models in § 6.2. However, under typical circumstances, this $t^* > 0$ information is unknown, and for this reason, $t^* = 0$ of the DNS is generally chosen as the LES IC.

The boundary conditions are periodic in the x_1 and x_3 homogeneous directions and non-reflective in the x_2 direction similar to that of DNS. The non-reflective boundary conditions, which were developed on the equivalent Euler equations (Okong'o & Bellan 2002*a*), do not explicitly involve the p-correction term (when operative). In these boundary conditions, p is that computed in LES, which, according to the SGS model, may or may not contain the p correction.

5. LES numerical methodology

The numerical method is essentially the same as in DNS (see § 3) so as to ensure that differences between LES and DNS are overwhelmingly due to the SGS models rather than the numerics. The LES grid must be fine enough to represent the mean initial profiles, and to resolve the large eddies, and coarse enough to necessitate SGS modelling and to show increase in computational efficiency. In this study, the choice is $\Delta x_{LES} = 4\Delta x_{DNS}$. This choice of grid resolution is justified by the energy spectra and by LES comparisons with the FC-DNS and with an LES devoid of SGS model, called the No Model case (see § 6.1). It is noteworthy that although the mathematical form of the equations for the No Model case is identical to the unfiltered equations, the meaning of the dependent variables is different, since the No Model computed solution is that of the filtered equations; the meaning of the variables is important when one wishes to compare simulation results with experimental data. Thus, even for the No Model case, the scientific target is to reproduce the FC-DNS; because of the identical form of the equations, one may consider the No Model case to be an under-resolved DNS, depending on the viewpoint of interest, and then it should be compared with the coarsened DNS. To study the influence of the grid size, an LES study with a finer grid ($\Delta x_{LES} = 2\Delta x_{DNS}$) is performed with and without SGS model (Appendix B). The LES using an SGS model and performed on this finer grid is shown to basically be numerically equivalent to an under-resolved DNS, although here also the meaning of the dependent variables is not the same as in DNS. This equivalence indicates that an LES on a grid finer than $\Delta x_{LES} = 4\Delta x_{DNS}$ does not require SGS modelling.

The grid and test filters have a cubic top-hat mathematical form (for which the filtered value is simply the integrated value over the filter width), being the only one consistent with easy interpretation of results when using a finite-difference scheme. The spatial discretization is the same sixth-order accurate compact scheme used in the DNS, and time integration is performed using a fourth-order explicit Runge–Kutta scheme. The $\bar{\Delta}$ width is a compromise between retaining the maximum amount of information in the resolved scales and minimizing the discretization-error influences. In order to limit numerical errors, $\bar{\Delta}/\Delta x_{LES}$ must be chosen according to the accuracy of the space discretization scheme, irrespective of the grid resolution. For a sixth-order Padé scheme, this ratio must be $\bar{\Delta} \geqslant 2\Delta x_{LES}$ (Ghosal 1996; Chow & Moin 2003),

and the present choice is $\bar{\Delta} = 2\Delta x_{LES}$, meaning that the smallest resolved eddy is represented by at least two grid points.

Time stability is ensured by applying an explicit high-order filter to the conservative variables in each spatial direction. Since the role of this filter is to remove any unphysical high-wavenumber information from the solution before it contaminates the lower-wavenumber scales (Kennedy & Carpenter 1994), it is sometimes advisable to use filtering at every time step of the time integration. For the well-resolved DNS grid, the frequency of the high-order filtering is not expected to alter the solution. For LES devoid of an SGS model, since the LES grid resolution is only sufficient to resolve the large scales, it is expected that the selected filtering frequency affects the solution. Preliminary two-dimensional and three-dimensional numerical experiments with the No Model LES using various filter orders and filtering frequencies and decreasing grid resolution showed that when applying the filter more often, the results diverged from the filtered DNS. (The fact that the No Model solution is obtainable indicates that to a certain extent, this high-order filter may act like an implicit SGS model.) Thus, in LES we applied the filtering with the largest allowable time window, every two time steps (any larger period results in noise build-up in p and dilatation fields). Moreover, unlike in DNS, the filtering is performed over the entire domain including the points at and close to the non-periodic boundaries, and the order of the filter is increased to 12 in the interior with sixth-order boundary closures. Finally, the Courant–Friedrichs–Levy (CFL) number was adjusted to 0.85 from the unity DNS value, in order to apply filtering with a large time window.

The filtering frequency was investigated by exploring its dependence on the SGS model. When an SGS model is employed, the maximum allowable filtering frequency increases and is larger for some SGS models than for others. As the filtering frequency increases, the numerical dissipation associated with it decreases. Basically, the choice of the filtering frequency is a compromise between ensuring that the overwhelming amount of information is retained in the solution and allowing the computation to proceed for long enough times. For sake of consistency, the same filtering frequency was used in all LES runs.

6. Results

Throughout the presented results, we distinguish between the solution of the LES equations (2.2)–(2.5) and (2.19), which is the conservative variable vector ϕ_{LES}, with the equivalent primitive variable vector $\psi_{LES} \equiv \psi(\phi_{LES})$ and the ideal (but presumably unachievable) LES solution represented by $\overline{\phi}$ computed from the FC-DNS and the corresponding vector $\overline{\psi} = \psi(\overline{\phi})$. As stated in § 1, ϕ_{LES} will be here compared to $\overline{\phi}$ at the LES grid nodes. We first inquire in § 6.1 into the performance of constant-coefficient SGS-flux models and also evaluate the effect of the FOC model (2.37) by using HN600 as the baseline study. Then, we transcend in § 6.2 the constant-coefficient LES conducted with a p correction by performing LES with dynamic-coefficient SGS-flux models combined with a p-correction model. At this juncture, we first assess the performance of the p-correction type model by comparing the SOC model (2.36) with the FOC model (2.37) and choose the best of these two models for all other LESs. Finally, the extent to which the FC-DNS irreversible entropy production is recovered in LES is addressed in § 6.3. The stringent goal here is to obtain in LES both spatial and temporal equivalence with the FC-DNS. Clearly, if the interest is only in statistical equivalence (Pope 2004), then a larger set of models than the ones recommended for reaching our stringent requirements would be available to the user.

Run	SGS Model: SGS-flux model	SGS Model: Pressure correction	CPU hours
SMC	SMC; (2.20) and (2.22)	None	3
GRC	GRC; (2.23)	None	3
SSC	SSC; (2.24)	None	16
SMCP	SMC; (2.20) and (2.22)	Included; (2.37)	9
GRCP	GRC; (2.23)	Included; (2.37)	10
SSCP	SSC; (2.24)	Included; (2.37)	22
No Model	None	None	3
DNS	None	None	667

TABLE 4. The name convention and time requirements to reach $t^* = 135$ for the LES and DNS runs for HN600. For all LES cases, the grid is $72 \times 84 \times 44$. CPU hours are an estimate: aggregate over parallel processors on an SGI Altix 3000 system.

6.1. *Constant-coefficient LES and effect of the pressure correction*

The SMC, GRC and SSC models are here used in LES with the calibrated coefficient values for $\bar{\Delta}/\Delta x_{DNS} = 8$ obtained from the corresponding DNS at the transitional time (see Selle *et al.* 2007) $t^* = 135$ as follows:

$$C_{SM} = 0.0579 \text{ and } C_{YO} = 0.2471, \quad \text{SMC}, \tag{6.1}$$

$$C_{GR} = 0.1193, \quad \text{GRC}, \tag{6.2}$$

$$C_{SS} = 0.5770 \text{ for } \widehat{\Delta} = 2\bar{\Delta}, \quad \text{SSC}. \tag{6.3}$$

To investigate the effect of the p correction, LESs are conducted first without and then with the FOC model. Hence, there are six SGS-flux-including LES runs analysed. The results are compared with both the FC-DNS results and the No Model LES. The comparison with the latter is as important as with the former, since it provides insight into the necessity of an SGS model. The comparisons involve the timewise evolution of important global quantities, as well as the rendition of selected flow-variable spatial distribution at the DNS transitional time. Table 4 lists the name convention used for HN600 LES runs and compares the computational time requirements of LES cases and DNS to reach the time station of the DNS transitional state.

6.1.1. *Evolution of the global quantities*

Figure 2 displays the time evolution of $\delta_m/\delta_{\omega,0}$, the resolved kinetic energy $E_K = \langle\langle \rho(u_i u_i/2)\rangle\rangle$, the domain-averaged positive spanwise vorticity $\langle\langle \omega_3^+ \rangle\rangle$ and the domain-averaged enstrophy $\langle\langle \omega_i \omega_i \rangle\rangle$ for LES runs along with the FC-DNS as the ideal LES and for the DNS run; $\delta_m/\delta_{\omega,0}$, presented in figure 2($a$), shows the mixing-layer growth, which is essentially the same for the DNS and the FC-DNS. Several regions of varying slopes are identified. The first region is the roll-up period epitomizing laminar growth and lasting up to $t^* = 25$. What follows is a region culminating with the the first pairing at $t^* = 50$ and a further increase with a higher $\delta_m/\delta_{\omega,0}$ rate indicating a faster growth because of turbulent mixing. A second pairing eventually occurs, after which the layer transitions to turbulence and eventually the mixing-layer growth slows down. All LESs, except for SMC and SMCP, agree well with the FC-DNS before the first pairing; this is to be expected, considering that turbulence is relatively subdued before the first pairing. After the first pairing, GRC, SMC and SMCP LESs predict a much thinner layer than the template; the p correction does not seem here effective

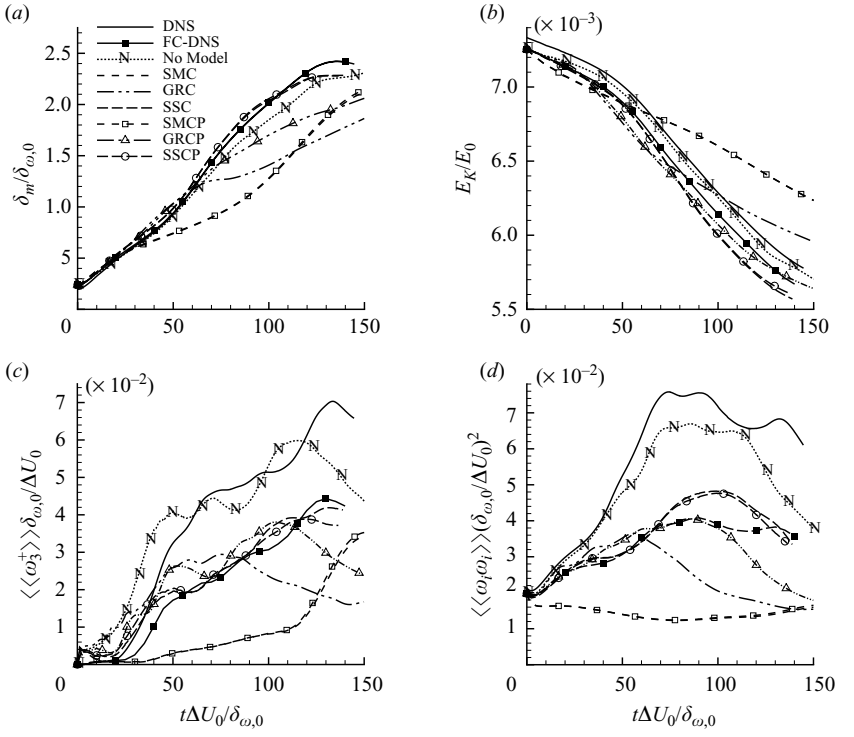

FIGURE 2. Time evolution of non-dimensional global quantities for HN600: (*a*) $\delta_m/\delta_{\omega,0}$, (*b*) E_K/E_0, (*c*) $\langle\langle\omega_3^+\rangle\rangle\delta_{\omega,0}/\Delta U_0$ and (*d*) $\langle\langle\omega_i\omega_i\rangle\rangle(\delta_{\omega,0}/\Delta U_0)^2$ for DNS, FC-DNS and LES listed in table 4; $E_0 = 452.076$ kJ is the initial total energy in the domain.

in mitigating the deficiencies of the SMC model. However, the *p*-correction model does delay the vortex breakdown in the GRC LES, and the GRCP is an improvement over the GRC, but even the GRCP model cannot fully recover from this discrepancy with the FC-DNS. Clearly, the SSC and SSCP LESs have the best agreement with the FC-DNS data. The comparison with the solution shows that none of the SMC, SMCP, GRC or GRCP models is an asset in the prediction of $\delta_m/\delta_{\omega,0}$; only SSC and SSCP overperform the No Model LES.

The time evolution of E_K/E_0 is displayed in figure 2(*b*). Filtering removes the SGS kinetic energy and results in a downshift for the FC-DNS compared with the DNS. However, the difference in kinetic energy between filtered and unfiltered DNS is small, being less than 3 %, with the maximum occurring at the DNS transition. The No Model case falls between the DNS and the FC-DNS and is considerably superior to either SMC or SMCP, both of which widely deviate from the FC-DNS template. The SMC model's characteristic dissipative nature overpredicts the energy decay at the early stages of the simulation and hinders turbulence development; thus, not having enough small scale structures, SMC underpredicts the energy decay after the first pairing. When supplemented with the *p* correction, the GRC model improves its performance, and after $t^* = 80$ it exhibits better agreement with the FC-DNS compared with the No Model case. Similar to the $\delta_m/\delta_{\omega,0}$ findings, both SSC and SSCP produce the best agreement with the FC-DNS, indicating that the amount of dissipation added with this model is adequate until $t^* = 80$. After $t^* = 80$, GRCP overperforms all other models.

Figure 2(*c*) illustrates $\langle\langle\omega_3^+\rangle\rangle\delta_{\omega,0}/\Delta U_0$, which, being initially null, measures the resolved small-scale activity; this activity experiences a sudden increase after roll-up. Filtering removes the smallest structures and thus considerably reduces $\langle\langle\omega_3^+\rangle\rangle\delta_{\omega,0}/\Delta U_0$ as clearly seen in figure 2(*c*). Understandably, the No Model simulation displays much larger values than the FC-DNS target solution, since the small structures are not subject to dissipative effects through SGS-flux models in that simulation, resulting in $\langle\langle\omega_3^+\rangle\rangle\delta_{\omega,0}/\Delta U_0$ being overpredicted. On the other hand, both SMC and SMCP underpredict $\langle\langle\omega_3^+\rangle\rangle\delta_{\omega,0}/\Delta U_0$ owing to their dissipative nature. The GRC model erroneously produces vorticity very early in the simulation, even before roll-up is finished, and eventually exhibits an earlier vorticity decay compared with the FC-DNS. To a certain extent, GRCP is an improvement of GRC, since the p correction delays the vorticity decay. The best agreement is obtained with SSC and SSCP, consistent with the $\delta_m/\delta_{\omega,0}$ and E_K findings.

Enstrophy is a measure of stretching and tilting effects, both of which instigate vorticity production. Plots of $\langle\langle\omega_i\omega_i\rangle\rangle(\delta_{\omega,0}/\Delta U_0)^2$ in figure 2(*d*) display results similar to $\langle\langle\omega_3^+\rangle\rangle\delta_{\omega,0}/\Delta U_0$. The best and worst overall agreements are obtained with the SSC or SSCP and the SMC or SMCP models, respectively, and the performance of GRC is considerably improved by the addition of the p correction included in GRCP.

Despite the fact that the No Model LES has better agreement with the DNS for these global measures than any of the other models, as already stated, from the LES viewpoint, the No Model target is the FC-DNS, not the DNS, and it is obvious that this simulation fails the most among all LESs in reaching the FC-DNS template. CPU times for all runs are listed in table 4 showing that all LESs have considerably reduced CPU times, boding well for LES utilization in practical applications. The No Model CPU time is similar to the smallest CPU time obtained with LES including only SGS-flux models. Finally, the SGS model embodied in the p correction either adds less than 40 % of CPU time (SSCP model versus SSC model) or increases the CPU time by factors of 2.7 (SMC versus SMCP) to 3.3 (GRC versus GRCP). However, even with the p correction, the CPU time is at a minimum a factor of 30 and at the maximum almost two orders of magnitude smaller than that for DNS, while the p-correction model improves the LES results considerably.

A global quantitative evaluation of the LES accuracy in predicting temporally mean values compared with the template FC-DNS can be obtained by defining, for any quantity of interest Ψ, relative errors

$$\varepsilon_{1,\Psi} = \frac{\sum_{l=0}^{l=N} |\langle\langle\Psi_{LES}(t_l)\rangle\rangle - \langle\langle\Psi_{FCDNS}(t_l)\rangle\rangle|}{\sum_{l=0}^{l=N} |\langle\langle\Psi_{FCDNS}(t_l)\rangle\rangle|}, \tag{6.4}$$

$$\varepsilon_{2,\Psi} = \frac{\displaystyle\int_0^{t_{tr}^*} ([\langle\langle\Psi_{LES}(t)\rangle\rangle - \langle\langle\Psi_{FCDNS}(t)\rangle\rangle]^2)\,\mathrm{d}t}{\displaystyle\int_0^{t_{tr}^*} [\langle\langle\Psi_{FCDNS}(t)\rangle\rangle]^2\,\mathrm{d}t} \tag{6.5}$$

computed according to the L1 and L2 norms (e.g. Meyer, Geurts & Baelmans 2003), where t_l represents the time at which the solution has been outputted. Both $\varepsilon_{1,\Psi}$ and $\varepsilon_{2,\Psi}$ can account for any deviations between each LES and the FC-DNS. Since $\delta_m/\delta_{\omega,0}$, E_K/E_0, $\langle\langle\omega_3^+\rangle\rangle\delta_{\omega,0}/\Delta U_0$ and $\langle\langle\omega_i\omega_i\rangle\rangle(\delta_{\omega,0}/\Delta U_0)^2$ are already domain-averaged quantities, they already represent $\langle\langle\Psi\rangle\rangle$. Listed in table 5 are ε_Ψ values

	$\delta_m/\delta_{\omega,0}$		E_K/E_0		$\langle\langle\omega_3^+\rangle\rangle\delta_{\omega,0}/\Delta U_0$		$\langle\langle\omega_i\omega_i\rangle\rangle(\delta_{\omega,0}/\Delta U_0)^2$	
Run	$\varepsilon_{1,\Psi}$	$\varepsilon_{2,\Psi}$	$\varepsilon_{1,\Psi}$	$\varepsilon_{2,\Psi}$	$\varepsilon_{1,\Psi}$	$\varepsilon_{2,\Psi}$	$\varepsilon_{1,\Psi}$	$\varepsilon_{2,\Psi}$
SMC	304	345	30	40	775	760	573	612
SMCP	299	341	30	41	767	755	570	608
GRC	200	253	13	16	444	400	249	317
GRCP	110	136	10	12	281	259	49	69
SSC	35	34	9	13	163	164	102	144
SSCP	37	36	9	12	169	180	94	130
No Model	64	73	11	12	1015	889	521	586

TABLE 5. Computed errors (in $\times 10^{-3}$) for LES with respect to the FC-DNS for different constant-coefficient SGS models according to (6.4) and (6.5).

for all constant-coefficient models and the No Model LES. Among $\varepsilon_{1,\Psi}$ and $\varepsilon_{2,\Psi}$ for the four quantities, errors associated with E_K/E_0 decay are smallest, while those for $\langle\langle\omega_3^+\rangle\rangle\delta_{\omega,0}/\Delta U_0$ are the most prominent, followed by $\langle\langle\omega_i\omega_i\rangle\rangle(\delta_{\omega,0}/\Delta U_0)^2$. The fact that both norms predict similar relative ordering of model accuracy is encouraging in terms of evaluating the models' capability. For both $\varepsilon_{1,\Psi}$ and $\varepsilon_{2,\Psi}$ the minimum error in $\langle\langle\omega_3^+\rangle\rangle\delta_{\omega,0}/\Delta U_0$ is for the SSC and SSCP models (for the SSC model, the p correction does not seem beneficial for this quantity) followed by the GRCP model, whereas the largest error is for the No Model LES, followed by SMC and SMCP. For $\langle\langle\omega_i\omega_i\rangle\rangle(\delta_{\omega,0}/\Delta U_0)^2$, both $\varepsilon_{1,\Psi}$ and $\varepsilon_{2,\Psi}$ indicate that the minimum error is for GRCP (which is considerably smaller than for GRC), followed by SSCP, while the largest error is for SMC followed by SMCP. With the exception of $\langle\langle\omega_3^+\rangle\rangle\delta_{\omega,0}/\Delta U_0$, for all other global quantities, $\varepsilon_{1,\Psi}$ and $\varepsilon_{2,\Psi}$ are larger for SMC and SMCP than for the No Model case, casting great doubts about the SMC and SMCP predictive capabilities for these temporally mean values. The p-correction model seems most effective for the GR model for which it reduces errors for $\langle\langle\omega_3^+\rangle\rangle\delta_{\omega,0}/\Delta U_0$ by approximately 40 % and by as much as approximately a factor of five for $\langle\langle\omega_i\omega_i\rangle\rangle(\delta_{\omega,0}/\Delta U_0)^2$.

6.1.2. *Flow visualizations*

To better understand the impact of the SGS models in reproducing the FC-DNS we turn to flow visualizations at $t^* = 135$. Although many dependent variables could be plotted, we focus here for obvious reasons on the vortical aspect of the flow, on $|\nabla\rho|$ because it directly influences the turbulence distribution in the flow field (Hannoun *et al.* 1988), on p because of its strong nonlinear relationship to other thermodynamic variables through the EOS and because a deficient p field implies inaccuracies in the velocity field through the momentum equation and on Y_h because its distribution is a manifestation of mixing.

Figure 3 illustrates $\omega_3\delta_{\omega,0}/\Delta U_0$ for all LESs. The No Model simulation displays more small-scale structures than can possibly be resolved on such a coarse grid, and the vortex strength is comparable to the FC-DNS data. The SMC and SMCP simulations show that the size of the large-scale vortex is well captured, but the vortex completely lacks small-scale structure. The GRC simulation has the thinnest layer among all LESs and also the weakest vorticity. The p correction, included in GRCP, restores some of the physics, as it enlarges the layer thickness and strengthens the vorticity intensity. The SSC simulation, especially after the p-correction addition embedded in SSCP, has the best agreement with the FC-DNS, although it predicts

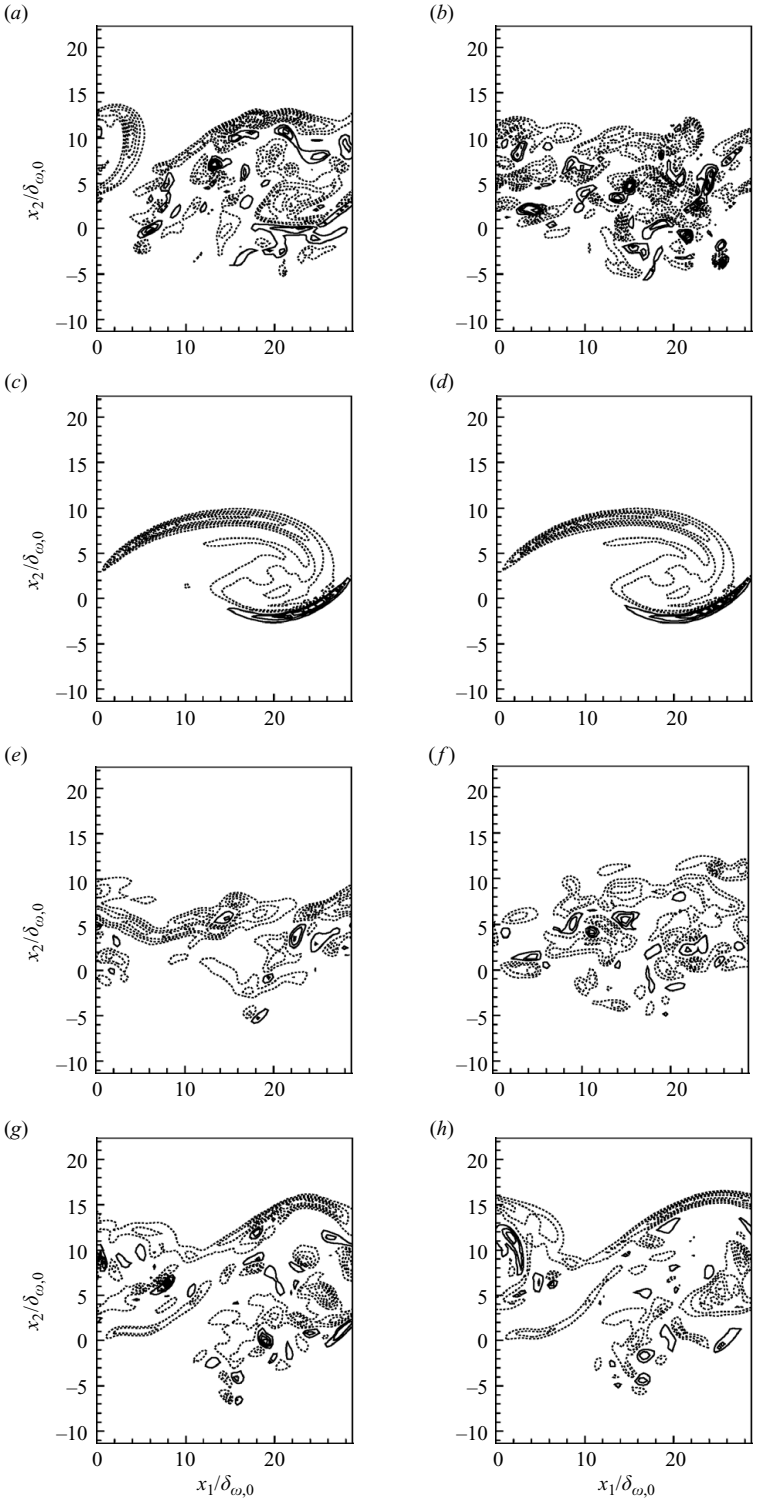

FIGURE 3. Spanwise vorticity $\omega_3\delta_{\omega,0}/\Delta U_0$ for HN600 at t^*_{tr} of the DNS ($t^* = 135$) in the between-the-braid plane ($x_3/L_3 = 0.06$): (*a*) FC-DNS; (*b*) No Model; (*c*) SMC; (*d*) SMCP; (*e*) GRC; (*f*) GRCP; (*g*) SSC; (*h*) SSCP. The solid lines denote positive values, and the dotted lines represent negative values. There are 12 contour levels ranging between −0.7 and 0.5.

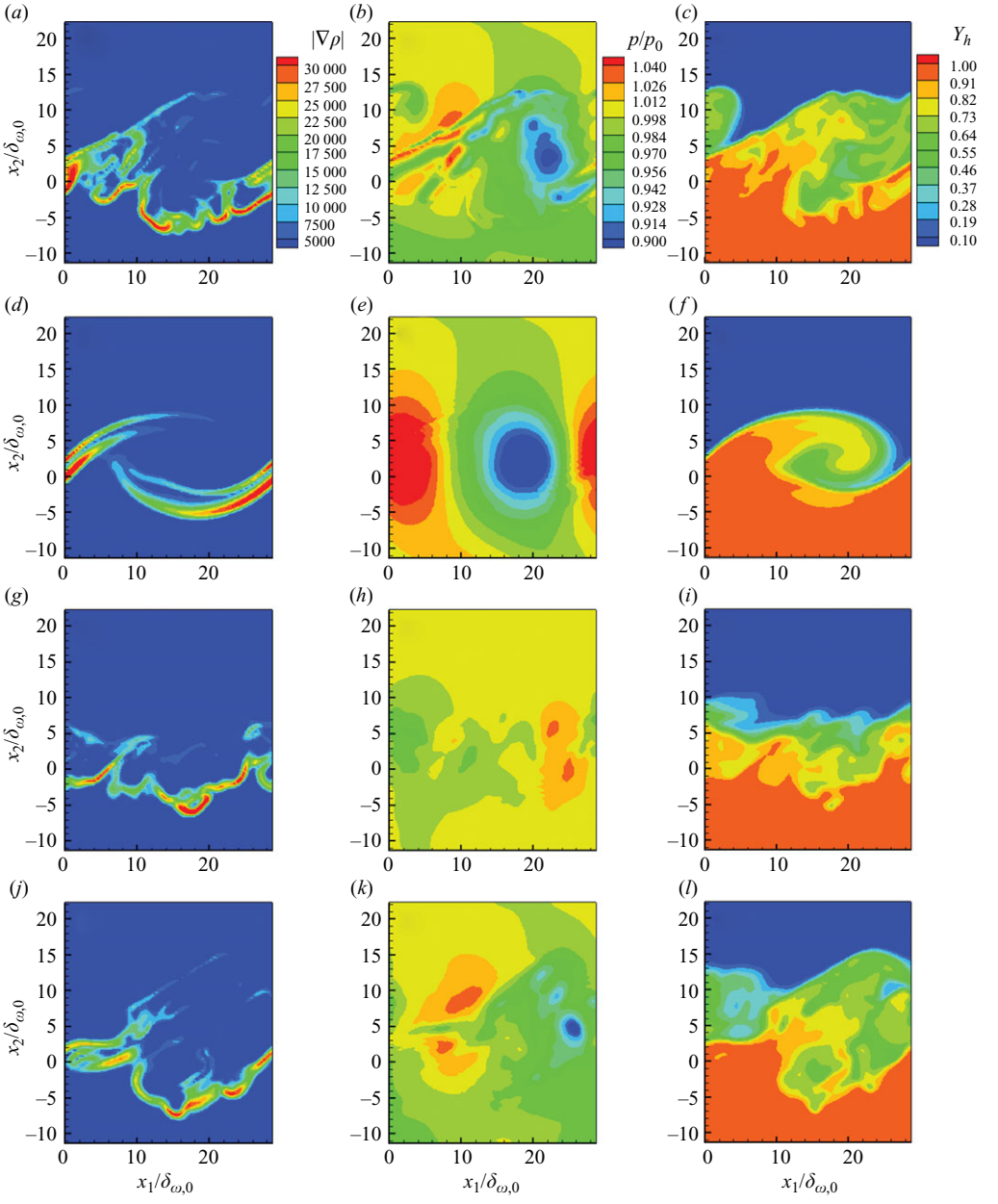

FIGURE 4. Comparison of $|\nabla\rho|$ in kg m^{-4} (first column), p/p_0 (second column) and Y_h (third column) for HN600 at t^*_{tr} of the DNS ($t^* = 135$) in the between-the-braid plane ($x_3/L_3 = 0.06$) for (*a*, *b*, *c*) FC-DNS, (*d*, *e*, *f*) SMC, (*g*, *h*, *i*) GRC and (*j*, *k*, *l*) SSC (SMC, GRC and SSC are devoid of the p correction).

an excessively large vortex size, a decreased structure and diminished vortical strength.

Figures 4 and 5 depict the $|\nabla\rho|$, p/p_0 and Y_h contour plots from the FC-DNS (figures 4*a*–4*c*) and all LESs at $t^* = 135$. The SMC model predicts well the large-scale behaviour but entirely lacks small structures, as indicated by smooth features seen in the contours of all $|\nabla\rho|$, p/p_0 and Y_h (figures 4*d*–4*f*). Lacking the resolved small-scale

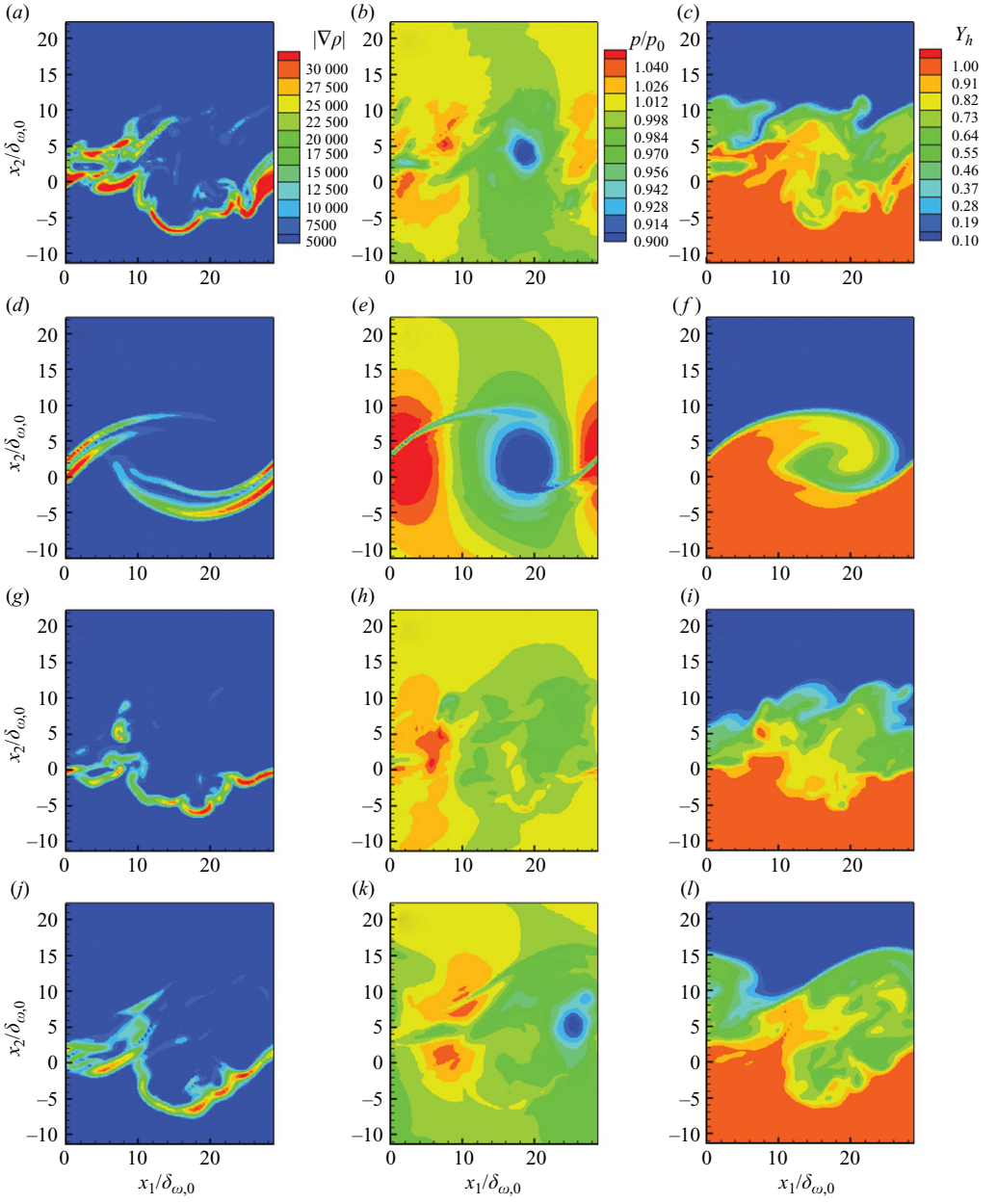

FIGURE 5. Comparison of $|\nabla\rho|$ in kg m^{-4} (first column), p/p_0 (second column) and Y_h (third column) for HN600 at t^*_{tr} of the DNS ($t^* = 135$) in the between-the-braid plane ($x_3/L_3 = 0.06$) for (*a*, *b*, *c*) No Model, (*d*, *e*, *f*) SMCP, (*g*, *h*, *i*) GRCP and (*j*, *k*, *l*) SSCP (SMCP, GRCP and SSCP include the p correction).

structure, it is not surprising that SMC captures to a certain extent the p/p_0 field, since it is precisely the presence of the small scales that necessitated the p correction. Because of the SM highly dissipative nature, the addition of the p correction (SMCP results in figures 5*d*–5*f*) does not significantly improve the predictive ability of SMC, although it does add some more realistic features to p/p_0. The GRC model exhibits considerably more small structures than SMC in both $|\nabla\rho|$ and Y_h contours (figures 4*g*

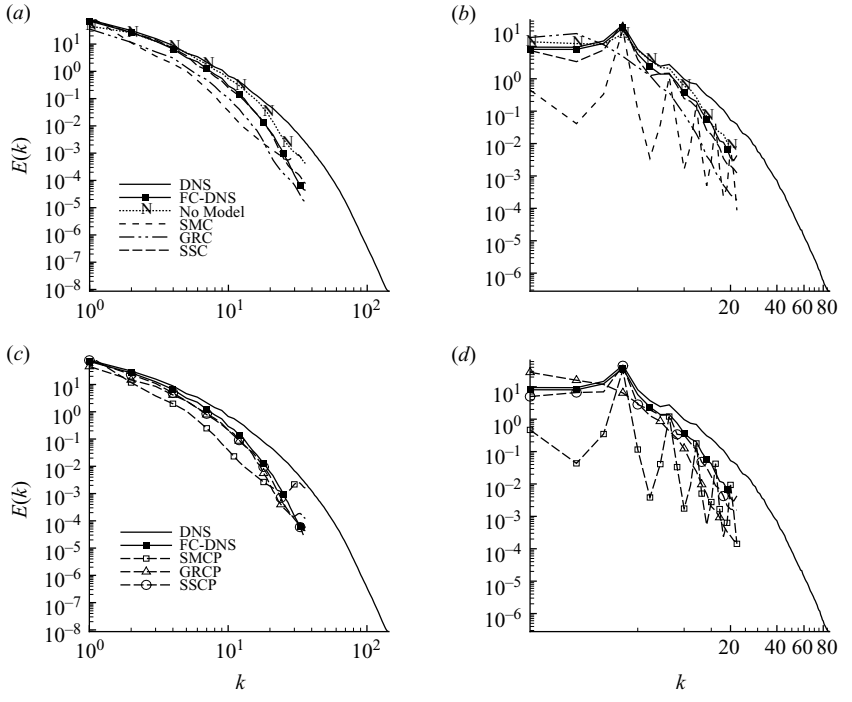

FIGURE 6. Energy spectra of u_1 for HN600 at $t^* = 135$: (a, b) without p correction and (c, d) with p correction; (a, c) streamwise and (b, d) spanwise. Energy in $m^2\ s^{-2}$.

and 4i), but its p/p_0 field (figure 4h) does not resemble at all that of the FC-DNS and in particular relatively misplaces the regions of low and high p/p_0. Adding the p correction improves considerably the solution (GRCP results in figures 5g–5i), in particular by having a correct relative placement of low- and high-p/p_0 regions, but deficiencies are still apparent. The second best results are obtained with the SSC model (figures 4j–4l), and the best solution is that of SSCP (figures 5j–5l) in that it captures substantial, although not all, the FC-DNS distinctive features of $|\nabla\rho|$, p/p_0 and Y_h but smoothes them out. Finally, the No Model simulation (figures 5a–5c) captures the $|\nabla\rho|$ location to a reasonable extent but overpredicts its magnitude and captures p/p_0 less well than it does $|\nabla\rho|$.

6.1.3. *One-dimensional spectra of the streamwise velocity*

Figure 6 displays the spanwise and streamwise energy spectra $E(k)$ of u_1 at $t^* = 135$. The plots show that the wavenumber range which must be resolved in LES is smaller than that of the DNS, as expected, since filtering removes the higher wavenumbers and reduces the energy content of the highest resolved wavenumber.

The streamwise spectra in figures 6(a) and 6(c) show that the No Model simulation has higher energy content than the FC-DNS throughout the spectrum because of excessive small-scale activity. The SMC model is the only one producing slightly higher energy content at the lowest wavenumbers and exhibiting lower energy for most of the spectrum, implying both inaccuracy at the large scales and lack of resolved small-scale activity. The GRC model deviates from the FC-DNS at all scales, with the exception of the smallest resolved scales. The SSC model reproduces reasonably well the streamwise spectral energy at the large scales. With the addition of the

p correction, there is an obvious improvement only for the GR model. The GRCP spectra agree well with those of FC-DNS, except for the largest resolved wavenumber at which they predict slightly more energy in small scales than the FC-DNS.

The striking feature of the spanwise spectra in figures 6(b) and 6(d) are the peaks exhibited by both SMC and SMCP, indicating that neither simulation has achieved transition at the DNS transitional time, in contrast to all other LESs. (The peak seen in the FC-DNS curve at $k = 4$ is attributed to spanwise forcing.) This information is consistent with the error analysis of § 6.1.1. The large-scale energy in SMC and SMCP is considerably smaller than in the FC-DNS, which is attributed to the models' dissipative nature. In contrast, GRC and GRCP show excess large-scale energy (more in GRCP) compared with the FC-DNS, with the opposite for SSC and SSCP. These findings are consistent with the results of figure 2, identifying vortical activity earlier in GRC and GRCP than in the FC-DNS.

6.2. *Dynamic-model LES with pressure correction*

The constant-coefficient LES study revealed that at one extreme is the SMC model, which displays unrealistically smooth contours but in which the central low-p-magnitude region does appear, albeit devoid of the correct FC-DNS structure. At the other extreme is the GRC model, which predicts small-scale structures (although the spatial distributions are only modestly reproducing the FC-DNS) but in which the computed p field is unlike that of the FC-DNS and where particularly the relative placement of low- and high-p/p_0 regions is incorrect. The SSC model is more successful at duplicating both the small-scale structure and the p/p_0 field. Basically, with the exception of SSC, the other SGS-flux models can modestly predict either $|\nabla\rho|$ or the p field but not both. Accepting a poor rendition of $|\nabla\rho|$ is not an option, since the HDGM regions strongly affect turbulence distribution by damping perpendicular modes and transmitting energy in the tangential direction (Hannoun *et al.* 1988). Furthermore, unlike in perfect-gas flows, here the thermodynamic variables are related through a strongly nonlinear EOS, and thus a small deviation in one of them from the FC-DNS can induce considerable deviations in the others, meaning that a poor rendition of the p field is not acceptable either; additionally, small inaccuracies in the p field induce large inaccuracies in the velocity field. Addition of the p-correction model mostly improves the GR model among similarity-based models, which is attributed to the fact that the model is precisely based on computing gradients, a computation that the p correction is meant to improve. The SS model also benefits from the p correction which introduces features more closely resembling that of the FC-DNS. The SM model is so dissipative that the small-scale structure introduced by the p correction is of little effect. Because the SSC and SSCP models show the best promise, the indication is that dynamic SGS-flux models, which inherently rely on the scale-similarity assumption, may be able to perform better than the constant-coefficient models.

Since the beneficial effect of a p-correction model has been established in § 6.1, all dynamic-coefficient LES include this additional SGS model. To evaluate the effectiveness of the FOC model versus the SOC model, LES are first conducted to this effect. The results identify FOC as being best, and thus the remaining LES are conducted with this model. The runs are listed in table 6, and all, with the exception of one, use $C_H(\varphi)$ of (2.31) with the multi-coefficient model of (2.32). These runs are performed with the SMD, the MGRD or the MSSD model of (2.30) or with the GRD model for which the computation is initialized either at $t^* = 0$ (GRDA-IC0) or at $t^* = 25$ (GRDA-IC25) to avoid the initial transients which produce problematic

Run	SGS Model		CPU hours
	SGS-flux model	Pressure correction	
SMD	SMD with $C_H(\varphi)$ of (2.31)	Included; (2.37)	19
MGRD-NPC	MGRD with $C_H(\varphi)$ of (2.31)	None	15
MGRD-FOC	MGRD with $C_H(\varphi)$ of (2.31)	Included; (2.37)	20
MGRD-SOC	MGRD with $C_H(\varphi)$ of (2.31)	Included; (2.36)	22
MSSD	MSSD with $C_H(\varphi)$ of (2.31)	Included; (2.37)	45
GRDA-IC0	GRD with $C_H(\varphi)$ of (2.31)	Included; (2.37)	22
GRDA-IC25	GRD with $C_H(\varphi)$ of (2.31)	Included; (2.37)	18
GRDV	GRD with $C_D(\varphi)$ of (2.31)	Included; (2.37)	20

TABLE 6. The name convention and time requirements to reach $t^* = 135$ for the LES runs using dynamic modelling for HN600. For all LES cases, the grid is $72 \times 84 \times 44$. CPU hours are an estimate: aggregate over parallel processors on an SGI Altix 3000 system.

SGS-flux coefficients, as discussed below. Therefore, not only are we comparing the performance of SGS models, but we are also assessing strategies on how they can best be used in conjunction with other aspects of the computation. The mixed models' motivation is not here the typical one in which the SM model is combined with either the GR or the SS model as a means to provide numerical stability to the computation; numerical stability is not a problem in the present LES, as shown by the ability to perform LES with the GRD model alone. Rather, the mixed models are here explored as a means of combining the attribute of the SM model to produce a good, although overstated, approximation of the p field with the feature of the GR or SS model to produce an understated p field but a good approximation of the $\nabla\rho$ field, which is lacking in the SM models. The idea is that a combination of SM and GR or SS may have the ultimate desirable characteristics of the FC-DNS; it is well known that transitional flows have substantial backscatter, and the $t^* = 135$ state may not be predictable without the backscatter capability of the GR or SS model. The only model in which $C_D(\varphi)$ (i.e. domain-averaged coefficients) of (2.31) was used is GRDV, and the motivation is, as for GRDA-IC25, the mitigation of some large SGS-flux coefficients produced in homogeneous planes during the initial p transients. In all dynamic models, $\hat{\Delta} = 2\bar{\Delta}$. The dynamic-coefficient models are evaluated in similar manner as the constant-coefficient models, that is to say by comparing them with the FC-DNS in terms of the global quantities, the important quantities $|\nabla\rho|$, p/p_0 and Y_h and the spectra.

Because the HN600 simulation is distinctive among the DNSs in table 3, in that it has the most prominent small-scale structure, it is instructive to inquire whether the performance of LES models examined so far extends to the FC-DNS obtained for other realizations. This topic is addressed in Appendix C.

6.2.1. *Assessment of the first-order versus the second-order p-correction model*

The SOC model for p is subject to the assumption of (2.35) and is described by (2.36) in which $(\partial^2 p/(\partial\phi_m\partial\phi_n))_{\phi=\overline{\phi}}$ is computed from the knowledge of $(\partial^2 p/(\partial\psi'_m\partial\psi'_n))_{\psi'=\overline{\psi'}}$ through the PR EOS as described by Selle *et al.* (2007) and where quantities $\vartheta(\overline{\phi_m}, \overline{\phi_n})$ are modelled using the GRD SGS-flux model described in § 2.4.1. The model is implemented in the code by computing in the momentum equation

$$\nabla(p(\overline{\phi})) + \nabla(\overline{p\,(\phi)} - p\,(\overline{\phi})) = \nabla(\overline{p\,(\phi)}) = \nabla\left[\overline{p\,(\overline{\phi})} + \frac{1}{2}\left.\frac{\partial^2 p}{\partial\phi_m\partial\phi_n}\right|_{\phi=\overline{\phi}} \vartheta(\overline{\phi_m}, \overline{\phi_n})\right]. \quad (6.6)$$

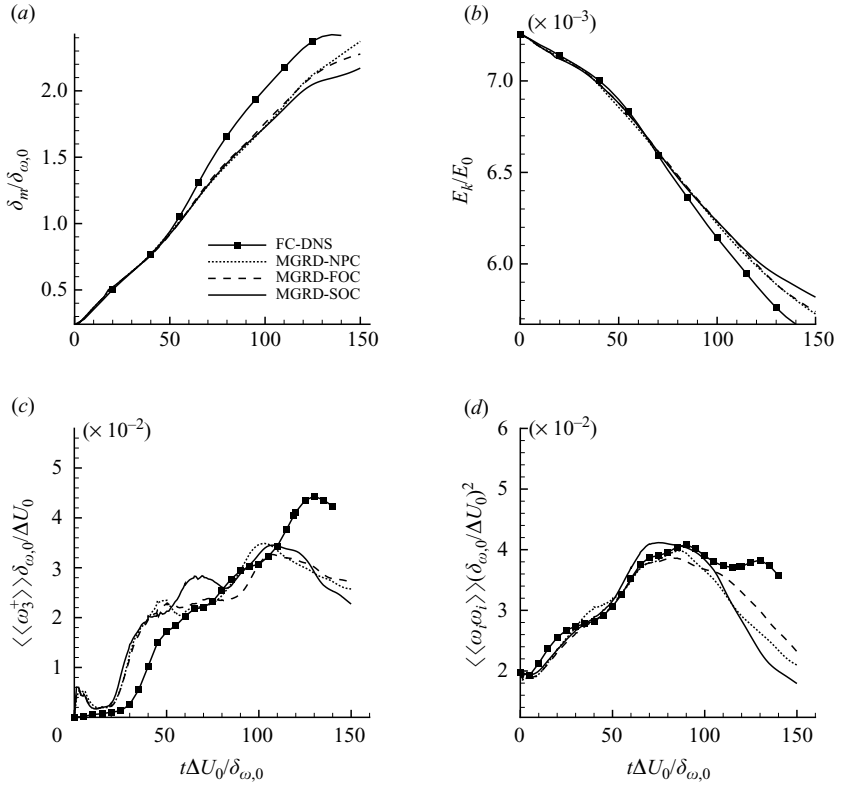

FIGURE 7. Time evolution of non-dimensional global quantities for HN600: (*a*) $\delta_m/\delta_{\omega,0}$, (*b*) E_K/E_0, (*c*) $\langle\langle\omega_3^+\rangle\rangle\delta_{\omega,0}/\Delta U_0$ and (*d*) $\langle\langle\omega_i\omega_i\rangle\rangle(\delta_{\omega,0}/\Delta U_0)^2$ for the no p correction (MGRD-NPC), first-order p correction (MGRD-FOC) and second-order p correction (MGRD-SOC); E_0 is the initial total energy in the domain.

The global-quantity results are presented in figure 7 for the LES conducted, as an example, with the MGRD model for the SGS fluxes and either with no p correction (NPC) or with FOC or SOC. The resolution is the same for all LESs, particularly $\bar{\Delta} = 8\Delta x_{DNS}$, which is the filter size at which Selle *et al.* (2007) found deterioration of the SOC model, as explained in § 2.4.2. Results depicted in figure 7 show that compared with the FOC, the SOC model is slightly inferior in duplicating $\delta_m/\delta_{\omega,0}$ and E_K/E_0 of the FC-DNS, seems somewhat inferior in reproducing the vortical features of the flow embedded in $\langle\langle\omega_3^+\rangle\rangle\delta_{\omega,0}/\Delta U_0$ and is clearly inferior in reproducing $\langle\langle\omega_i\omega_i\rangle\rangle(\delta_{\omega,0}/\Delta U_0)^2$; more quantitative conclusions using $\varepsilon_{1,\Psi}$ and $\varepsilon_{2,\Psi}$ are presented in table 7 and discussed in conjunction with similar results for the other dynamic models in § 6.2.2. Compared with the LES exercised with the MGRD model but NPC, both LESs with the p-correction model show better predictive capabilities. Flow visualizations presented in § 6.2.3 reinforce these conclusions. Therefore, the FOC model will be used for all other LESs below.

6.2.2. *Evolution of the global quantities*

Figure 8 displays the time evolution of $\delta_m/\delta_{\omega,0}$, E_K/E_0, $\langle\langle\omega_3^+\rangle\rangle\delta_{\omega,0}/\Delta U_0$ and $\langle\langle\omega_i\omega_i\rangle\rangle(\delta_{\omega,0}/\Delta U_0)^2$ for the FC-DNS data and for all LESs performed with SGS-flux dynamic models and the FOC model for p. The SMD model performs considerably better compared with the SMC model presented in figure 2; $\delta_m/\delta_{\omega,0}$

Run	$\delta_m/\delta_{\omega,0}$		E_K/E_0		$\langle\langle\omega_3^+\rangle\rangle\delta_{\omega,0}/\Delta U_0$		$\langle\langle\omega_i\omega_i\rangle\rangle(\delta_{\omega,0}/\Delta U_0)^2$	
	$\varepsilon_{1,\Psi}$	$\varepsilon_{2,\Psi}$	$\varepsilon_{1,\Psi}$	$\varepsilon_{2,\Psi}$	$\varepsilon_{1,\Psi}$	$\varepsilon_{2,\Psi}$	$\varepsilon_{1,\Psi}$	$\varepsilon_{2,\Psi}$
SMD	179	201	18	24	344	330	227	263
MGRD-NPC	98	122	5	7	206	235	50	64
MGRD-FOC	91	112	6	8	211	225	41	48
MGRD-SOC	100	123	6	8	244	258	46	59
MSSD	53	64	4	5	363	365	175	198
GRDA-IC0	99	131	6	8	318	289	60	79
GRDA-IC25	42	59	6	8	183	202	96	142
GRDV	83	107	8	10	330	290	46	54

TABLE 7. Computed errors (in $\times 10^{-3}$) for LES with respect to the FC-DNS for different dynamic-coefficient SGS models according to (6.4) and (6.5).

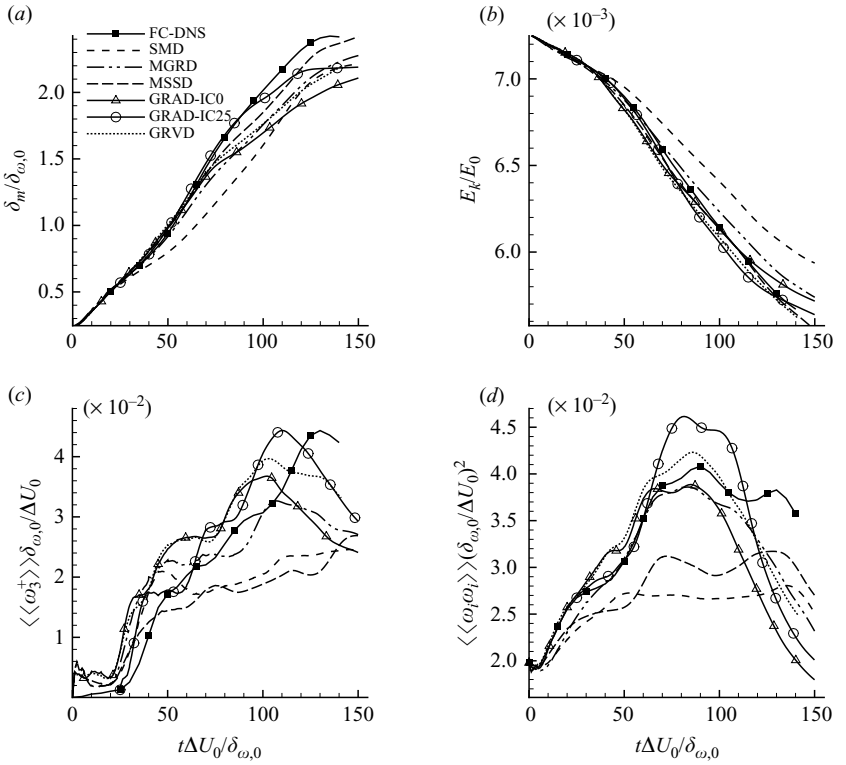

FIGURE 8. Time evolution of non-dimensional global quantities for HN600 computed with dynamic SGS modelling: (*a*) $\delta_m/\delta_{\omega,0}$, (*b*) E_K/E_0, (*c*) $\langle\langle\omega_3^+\rangle\rangle\delta_{\omega,0}/\Delta U_0$ and (*d*) $\langle\langle\omega_i\omega_i\rangle\rangle(\delta_{\omega,0}/\Delta U_0)^2$ for FC-DNS and LES listed in table 5.

and E_K/E_0 evolutions are closer to that of the FC-DNS, and $\langle\langle\omega_3^+\rangle\rangle\delta_{\omega,0}/\Delta U_0$ and $\langle\langle\omega_i\omega_i\rangle\rangle(\delta_{\omega,0}/\Delta U_0)^2$, which were substantially underestimated in constant-coefficient runs, are here more realistic. When the SM model is used in conjunction with the GR or SS model, both $\delta_m/\delta_{\omega,0}$ growth and E_K/E_0 decay are better predicted, particularly at the earlier times, and better with MSSD than MGRD. The MGRD model predictions for both $\langle\langle\omega_3^+\rangle\rangle\delta_{\omega,0}/\Delta U_0$ and $\langle\langle\omega_i\omega_i\rangle\rangle(\delta_{\omega,0}/\Delta U_0)^2$ are much closer to the FC-DNS

than those of the SMD model. Compared with the MGRD results, those of the MSSD are considerably inferior for both $\langle\langle\omega_3^+\rangle\rangle\delta_{\omega,0}/\Delta U_0$ and $\langle\langle\omega_i\omega_i\rangle\rangle(\delta_{\omega,0}/\Delta U_0)^2$. Thus, among eddy-viscosity-based dynamic models, the best agreement with the FC-DNS in predicting vortical flow features is achieved by MGRD, while the CPU time is similar to the much worse SMD model (see table 6).

In implementing the dynamic modelling for the GR model it was observed that the dynamically computed coefficient values were too large to be physically acceptable at the very early stages of the simulations, where the flow is laminar and no significant contributions from the SGS fluxes are expected. Hence, a limiter was set, and all the coefficients were kept below a pre-specified value of 0.30. This value has a large margin over the theoretical value of 1/12 for the GR model. Unlike for the SM model, there is no clear improvement on GR predictive abilities when dynamic modelling is applied. For all four global quantities examined, the results of GRDA-IC0 are worse than those of GRCP. Although the vortical features of the flow are better predicted with this model compared with the eddy-viscosity-based models, there is an unexpected sudden decrease in the $\delta_m/\delta_{\omega,0}$ prediction. Previous authors (e.g. Vreman *et al.* 1996*b*; Berselli, Iliescu & Layton 2006) have reported the GR model to be numerically unstable; however, other authors used it successfully for both single-phase and two-phase flow LESs of temporal mixing layers (e.g. Leboissetier *et al.* 2005). Because the GRC simulations of § 6.1 showed that the GR model is very sensitive to the p correction, the conjecture is here that the poor performance of the GRDA-IC0 model may be due to the initial p-transients, which can be very substantial (Okong'o & Bellan 2002*b*). To avoid these p-transients, consistent with information discussed in Appendix A, the GRDA-IC25 simulation was conducted. This strategy led to considerably improved results as can be seen in figure 8. Another strategy for avoiding the full impact of the initial excessive value of dynamically computed coefficients in some of the homogeneous planes was to domain-average the computed coefficient (GRDV; earlier defined), leading similarly to results superior to GRDA-IC0, as portrayed in figure 8.

Figure 9 displays the evolution of the model coefficients in the $x_2 = 0$ plane. Figures 9(*a*)–9(*c*) are for the eddy-viscosity-based models with four coefficients, $C_{\tau d}$, $C_{\tau x}$, C_ζ, C_η. Figures 9(*d*)–9(*f*) are for GRD with three coefficients, C_τ, C_ζ, C_η. The YO coefficients of the SMD and MGRD models, $C_{\tau d}$, behave similarly: they are initially larger than 0.8, fall sharply to 0.20 by $t^* = 30$ and then increase to their maximum value of 0.30 around $t^* = 80$ (figures 9*a* and 9*b*). On the other hand, $C_{\tau d}$ of the MSSD model does not have unphysically large initial values (figure 9*c*). The values of the coefficients confirm that among SM-based models, the most dissipative model is the SMD model, having the largest coefficients, followed by the MSSD and the MGRD models. The indication is that the favourable predictions of MSSD are due to its effectiveness in eliminating the unphysical values of the YO coefficient that are observed at the beginning of the simulation. Although the SM-based models overcome these unrealistic high-coefficient values, the GR model is incapable of surmounting these initial difficulties. To illustrate the difficulty encountered in GRD models with large coefficients for $t^* < 25$ and the stabilization of their values with time, C_τ, C_ζ and C_η are shown in figure 9 in the $x_2 = 0$ plane, for GRDA-IC0, GRDA-IC25 and GRDV (figures 9*d*–9*f*), respectively. For GRDA-IC0, all three coefficients start from the pre-specified limiting value of 0.30 (not shown) and decline to approximately 0.10 within the roll-up period ($t^* = 25$). The maximum coefficient value is reached just after the first pairing and at transition for C_τ and C_η, and at transition for C_ζ. The maximum values for C_τ, C_ζ and C_η after the roll-up period are approximately 0.13,

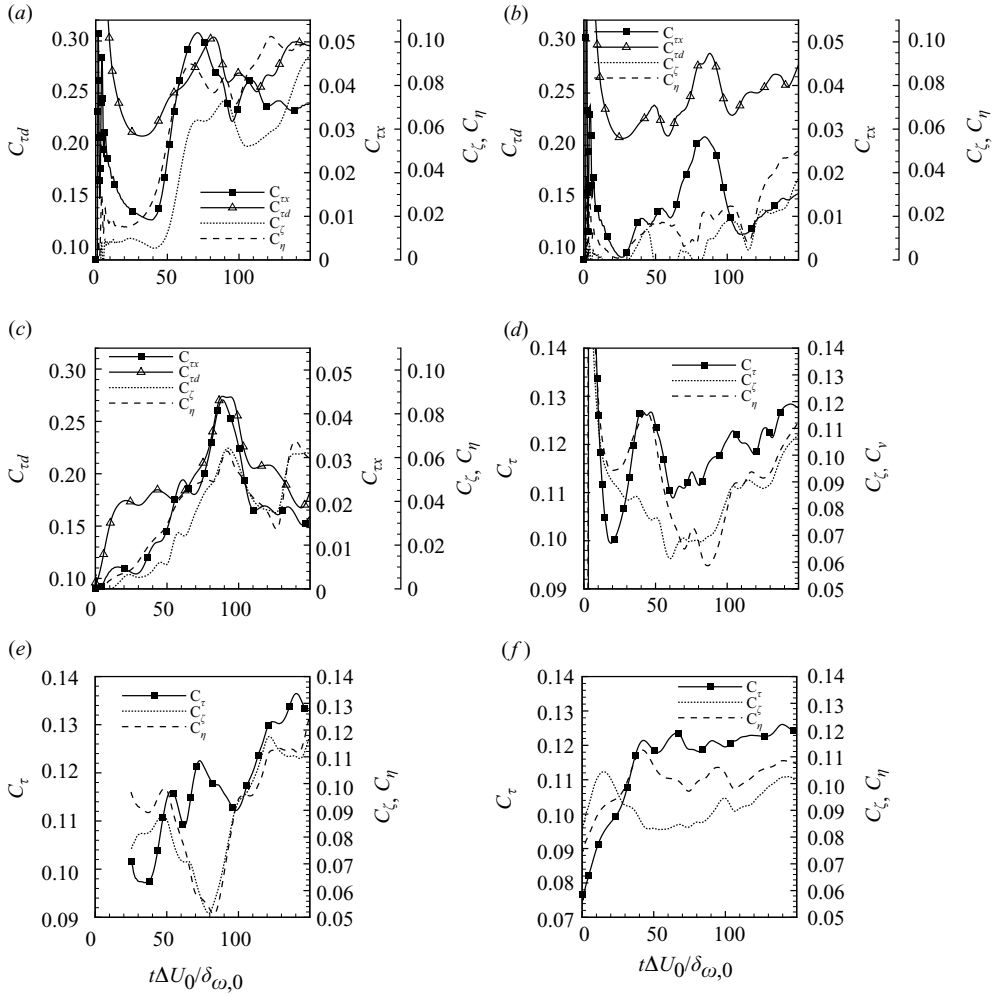

FIGURE 9. Evolution of the model coefficients of (*a*) SMD, (*b*) MGRD, (*c*) MSSD, (*d*) GRDA-IC0, (*e*) GRDA-IC25 and (*f*) GRDV for HN600 at $x_2 = 0$.

0.10 and 0.10, respectively (figure 9*d*). For both GRDA-IC25 and GRDV, the initially high-coefficient values were successfully avoided.

Results from an error analysis similar to that of § 6.1.1 are listed in table 7. Compared with error values listed in table 5, the errors are here considerably reduced, even for SMD, which is the most inaccurate dynamic LES according to these evaluations. Similar to the findings for constant-coefficient LES, errors associated with E_K/E_0 decay are smallest in the group, and for dynamic LES they are negligible. Although errors for $\langle\langle\omega_3^+\rangle\rangle\delta_{\omega,0}/\Delta U_0$ remain the most prominent, by difference from constant-coefficient LES, they are followed in magnitude by errors in $\delta_m/\delta_{\omega,0}$. Of note is that the SSCP model errors in $\langle\langle\omega_3^+\rangle\rangle\delta_{\omega,0}/\Delta U_0$ are smaller than all dynamic-coefficient LES errors in this quantity. The worst models are the GRDV, MSSD and SMD models, not necessarily ranked in the same order according to $\varepsilon_{1,\Psi}$ and $\varepsilon_{2,\Psi}$. By starting the LES at $t^* = 25$, one improves the accuracy. Considering both $\varepsilon_{1,\Psi}$ and $\varepsilon_{2,\Psi}$, SSCP is also the best model in predicting $\delta_m/\delta_{\omega,0}$, while the worst predictions among dynamic-coefficient models are obtained with the SMD LES, which is also the

worst for reproducing $\langle\langle\omega_i\omega_i\rangle\rangle(\delta_{\omega,0}/\Delta U_0)^2$. The most favourable $\langle\langle\omega_i\omega_i\rangle\rangle(\delta_{\omega,0}/\Delta U_0)^2$ predictions are by the MGRD-FOC, while SMD produces the worst ones. Generally, all three MGRD models (MGRD-NPC, MGRD-FOC and MGRDS-SOC) have relatively similar errors when compared with the other models, indicating that the error is associated with the MGRD attributes rather than with the type of the p correction.

6.2.3. *Flow visualizations*

Figure 10 displays the $|\nabla\rho|$, p/p_0 and Y_h distributions at $t^* = 135$ obtained with each of the LESs using dynamic models, except GRDV; the GRDV model was omitted because it exhibits similar behaviour as, although somewhat less successful than, GRDA-IC25. The idea of combining the SM model with the GR or SS model to mitigate the overprediction of p/p_0 from the former model with the underprediction of the latter, and to incorporate the advantageous small-scale reproduction of the latter models, was successful to a certain extent in that MGRD of figures 10(d)–10(f) is a better representation of the FC-DNS of figures 4(a)–4(c) than either SMD of figures 10(a)–10(c) or GRD of figures 10(j)–10(l). Between mixed models, MGRD is better than MSSD, which is attributed to the more acute underprediction of p/p_0 in GRCP than in SSCP that balances the strong overprediction of p/p_0 in SMCP and to the higher production of small scales in GRCP than in SSCP. Nevertheless, because of their strong dissipative behaviour, all SM-based (i.e. eddy-viscosity) models produce flows which are too smooth compared with the FC-DNS. On the other hand, GRDA-IC25 (see figures 10m–10o) successfully captures these structures while also giving a reasonable approximation – only slightly inferior to that of MSSD – of the FC-DNS p/p_0, showing that success in LES is not only determined by the SGS models but also by the ICs.

When examining the flow visualizations of figure 11 for the NPC and SOC models and comparing them with figures 10(d)–10(f), the conclusion is that the SOC model is slightly inferior in replicating the detailed structure of the flow. Computationally, the utilization of the SOC model also comes at a small additional cost: 22 CPU hours compared to the 20 hours of the FOC model, that is to say a 10 % increase in CPU time. The flow visualizations are consistent with the global-quantity results in that LES with the same dynamic SGS-flux model but NPC model is inferior to LES with either of the p-correction approaches, lacking some of the low-pressure regions and introducing spurious large-pressure regions while at the same time not providing a significant CPU-time computational saving having required 15 CPU hours.

6.2.4. *One-dimensional spectra of the streamwise velocity*

The interest in achieving in LES both temporal and spatial duplication of DNS prompts an examination of the velocity-fluctuation-based energy spectra at $t^* = 135$, illustrated in figure 12. The streamwise spectra of figure 12(a) show that the MGRD model predicts a more energetic flow at the small scales, having higher energy content than that of FC-DNS at the highest wavenumber. The MSSD displays the opposite behaviour, and similar to MGRD it has at the largest scale a lower energy content than the FC-DNS. The SMD model predicts a reduced energy with respect to the FC-DNS for all wave-numbers, except for the largest scale. The spanwise spectra of figure 12(b) indicate that neither SMD nor MSSD LES has reached a transitional state, as clearly seen by the numerous peaks (other than that of the initial perturbation) over the entire range of scales. Moreover, these two models also substantially underestimate (for SMD, up to two orders of magnitude) the energy

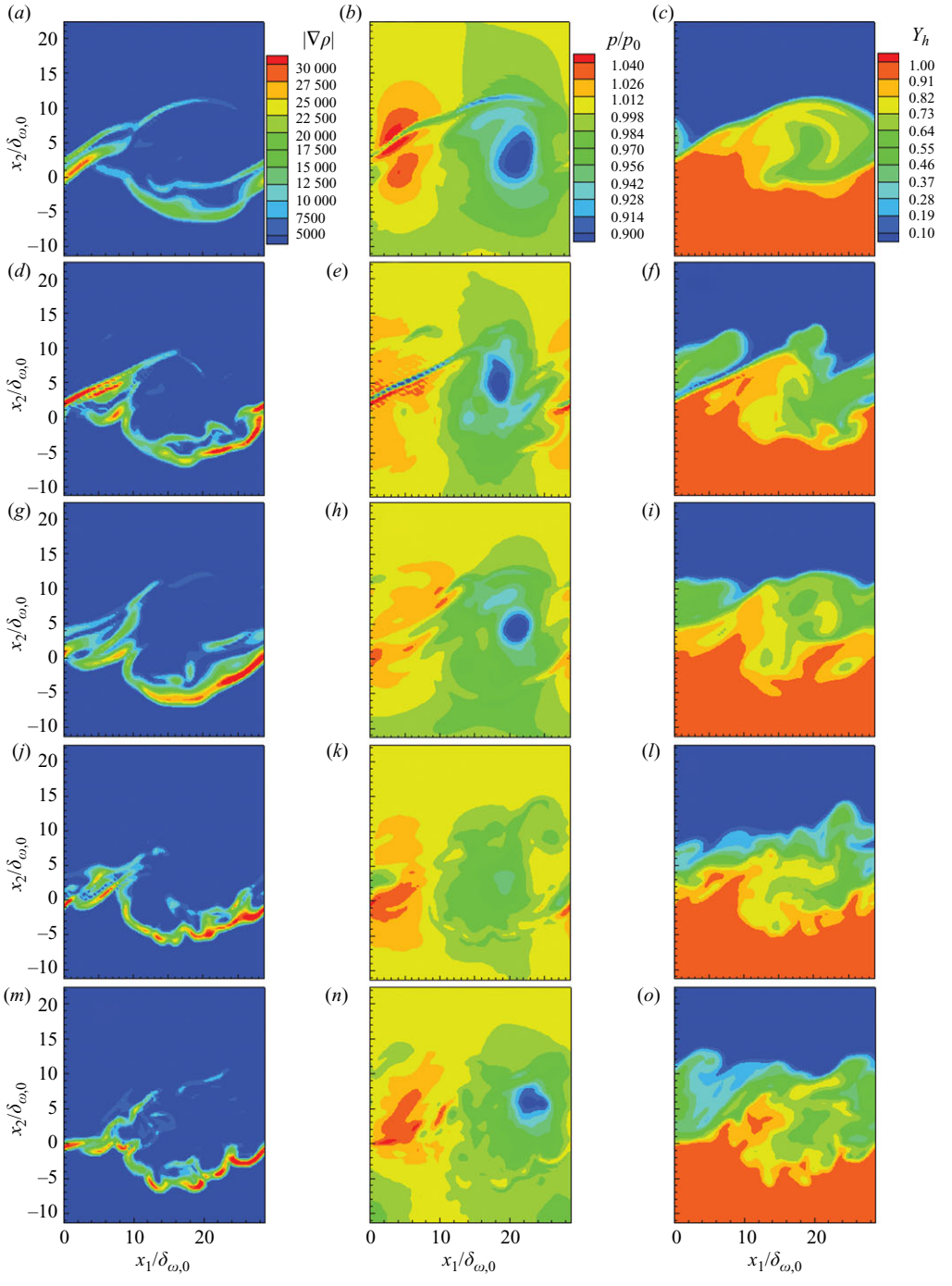

FIGURE 10. Comparison of $|\nabla\rho|$ in kg m^{-4} (first column), p/p_0 (second column) and Y_h (third column) for HN600 at t^*_{tr} of the DNS ($t^* = 135$) in the between-the-braid plane ($x_3/L_3 = 0.06$) for (*a*, *b*, *c*) SMD, (*d*, *e*, *f*) MGRD, (*g*, *h*, *i*) MSSD, (*j*, *k*, *l*) GRDA-IC0 and (*m*, *n*, *o*) GRDA-IC25. All models include the p correction.

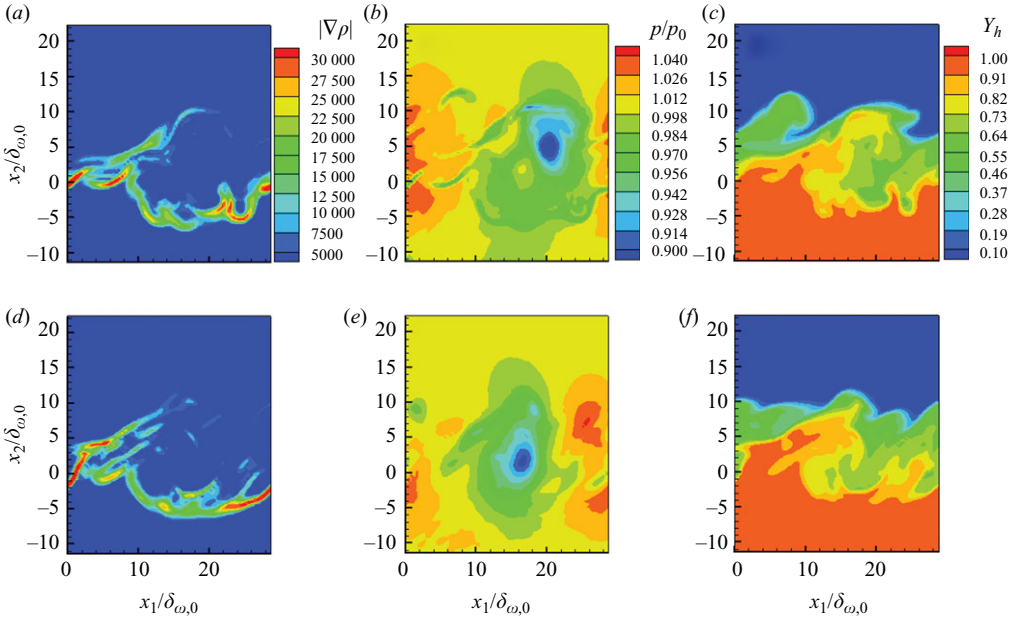

FIGURE 11. Flow visualizations comparing the MGRD using (*a*, *b*, *c*) the second-order p correction (MGRD-SOC) with MGRD using (*d*, *e*, *f*) no p correction (MGRD-NPC). Results are for $|\nabla\rho|$ in kg m^{-4} (first column), p/p_0 (second column) and Y_h (third column) for HN600 at t^*_{tr} of the DNS ($t^* = 135$) in the between-the-braid plane ($x_3/L_3 = 0.06$).

in the large scales. In contrast, the MGRD LES slightly overestimates the energy in the large scales and underestimates it in the small scales. Figure 12(*c*) indicates that for the largest scales of the spanwise spectra, GRDA-IC0 and GRDV are the most dissenting representations of the FC-DNS; however, the agreement at the smaller scales is very good. Similarly, the spanwise spectra of the dynamic gradient models (figure 12*d*) overestimate the energy content at both large and small scales.

6.3. *Irreversible entropy production*

The above results focused on primitive variables, which are the primary interest for flow predictions; however, we wish to highlight here the scientific information embedded in a higher-order quantity such as the irreversible entropy production which is essentially the dissipation (Hirshfelder *et al.* 1964); the dissipation is not to be confused with the TKE dissipation, as stated in § 1. Okong'o & Bellan (2000) have discussed in detail the irreversible entropy production concept and have shown that in the present situation the dissipation is the sum of three terms, each corresponding to a dissipation mode,

$$g_{tot} = g_{visc} + g_{temp} + g_{mass}, \tag{6.7}$$

with

$$g_{visc} = \frac{\mu}{T} 2 \left(S_{ij} - \frac{1}{3} S_{kk} \delta_{ij} \right)^2, \quad g_{temp} = \frac{\lambda}{T^2} \frac{\partial T}{\partial x_i} \frac{\partial T}{\partial x_i}, \quad g_{mass} = \frac{1}{Y_1 Y_2 \rho D} \frac{R_u m}{m_1 m_2} j_{2i} j_{2i}, \tag{6.8}$$

where g_{visc}, g_{temp} and g_{mass} represent contributions from the viscous, heat-flux and mass-flux modes, respectively. Different g_{tot} modes may be more prominent in various situations. For example, Okong'o & Bellan (2004*a*) have shown that in a compressible

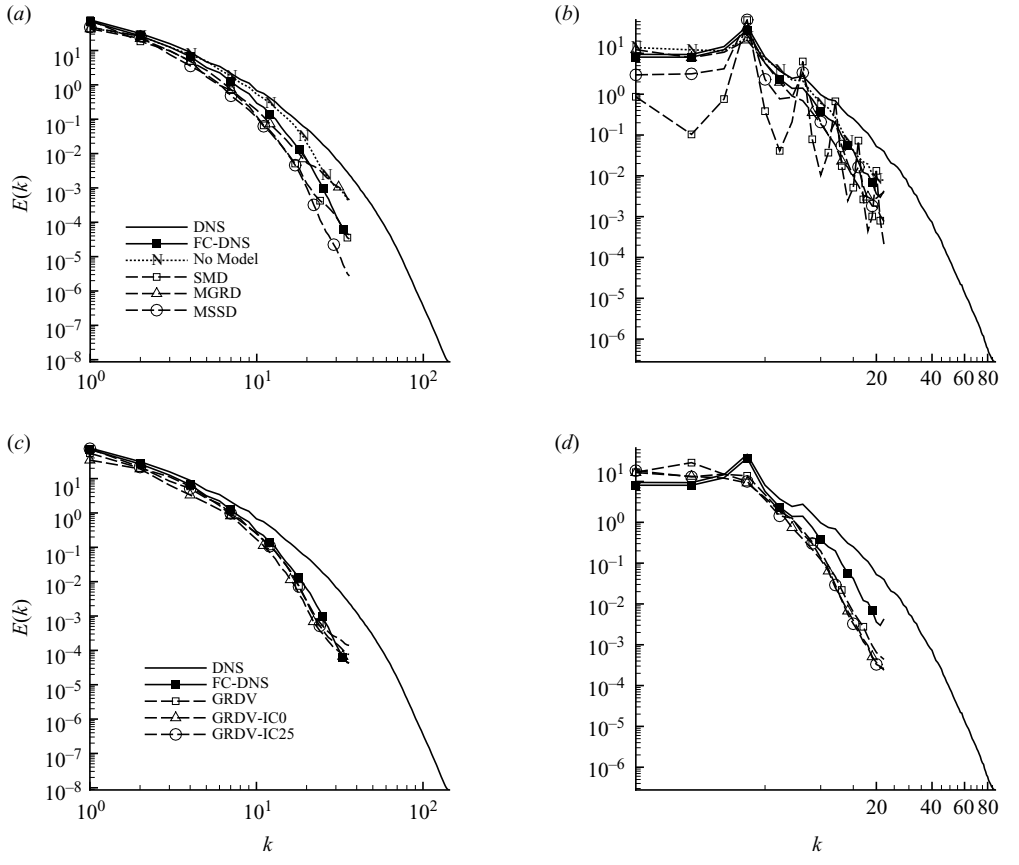

FIGURE 12. Energy spectra of u_1 for HN600 at $t^* = 135$ (a, b) with Smagorinsky-based dynamic models and (c, d) with similarity-based dynamic models; (a, c) streamwise and (b, d) spanwise. Energy in $m^2\ s^{-2}$.

atmospheric-p transitional shear layer, g_{tot} is dominated by g_{visc}, with negligible g_{temp}. However, unlike for atmospheric-p turbulent flows, in situations in which $p > p_c$, g_{tot} is dominated by g_{mass} with moderate contribution from g_{temp} and negligible portion from g_{visc}; this situation prevailed for both HN layers (Okong'o & Bellan 2002*b*) and OH layers (Okong'o *et al.* 2002). The prominence of g_{mass} is a direct consequence of the HDGM regions, and since the HDGM regions are a feature of fully turbulent $p > p_c$ flows, the dominance of g_{mass} in g_{tot} is expected to remain at high Re values.

Because filtering of the entropy equation does not introduce additional source terms, the comparison for evaluating LES predictions is between $g_k(\overline{\phi})$, where k is $visc$, $temp$ or $mass$ computed with $\overline{\phi}$ being either the FC-DNS field or the LES field. Results are depicted in figure 13 as the time variation of the domain-averaged values of each mode for LES compared with the equivalent results from the FC-DNS, all normalized by the maximum DNS value found for each mode. Figures 13(a), 13(c) and 13(e) show the temporal variation observed in the eddy-viscosity-based dynamic models for viscous, heat-flux and mass-flux modes, respectively. The MGRD model, whether or not used in combination with a p correction, is clearly superior to the MSSD and SMD models in capturing the g_{visc} FC-DNS result (figure 13a). Until close to transition, this model overpredicts both g_{temp} and g_{mass}, but by $t^* = 100$ there is an underprediction for g_{temp}, while the values for g_{mass} are excellent; in comparison, both SMD and MSSD estimates are low with respect to the FC-DNS

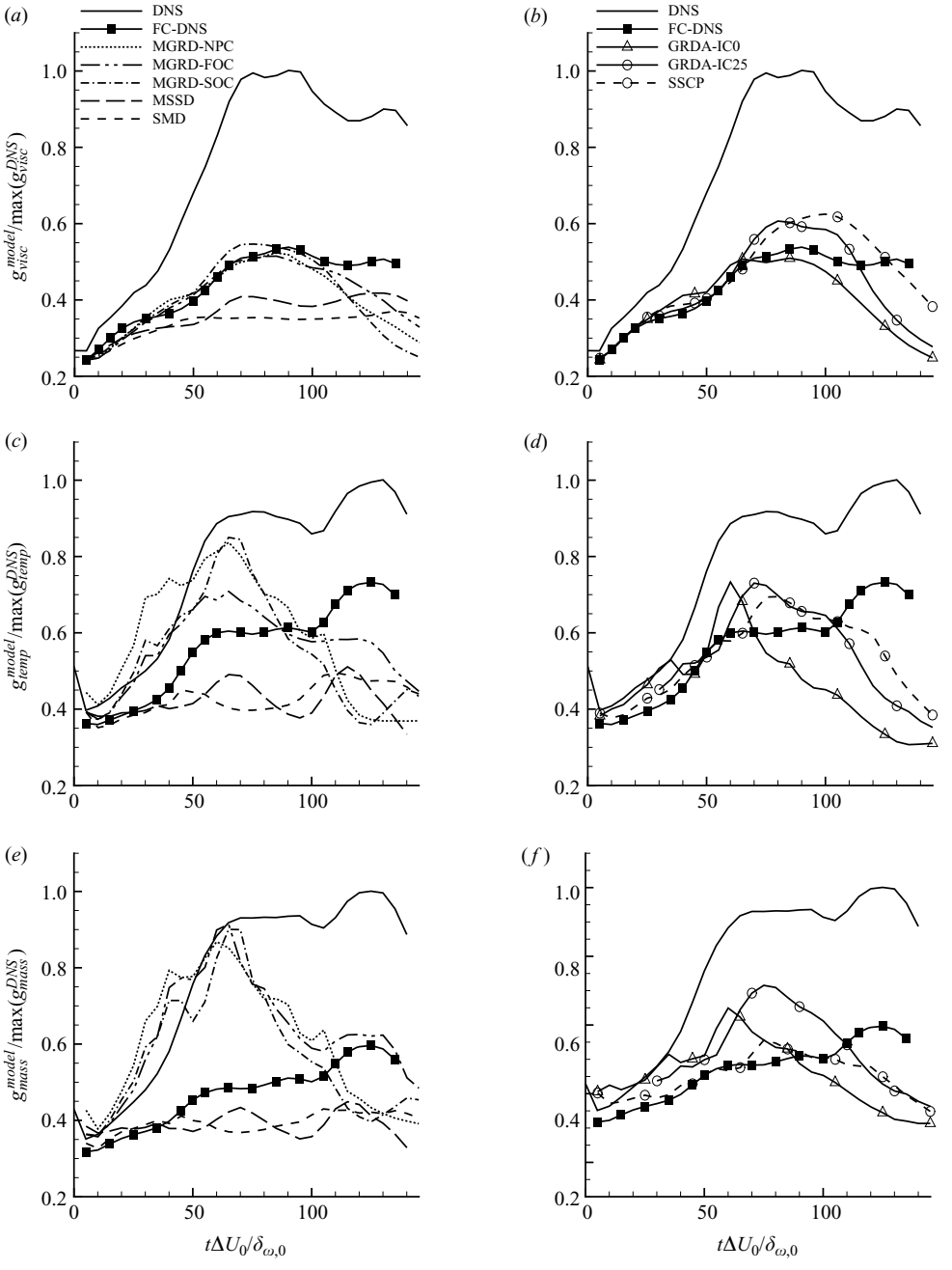

FIGURE 13. Time evolution of the domain-averaged irreversible entropy production for HN600 as computed from FC-DNS and (*a*, *c*, *e*) LES with eddy-viscosity-based dynamic models (SMD, MGRD, MSSD, MGRD-SOC, MGRD-NPC), (*b*, *d*, *f*) LES with dynamic GR model initiated from $t^* = 0$ (GRDA-IC0) and $t^* = 25$ (GRDA-IC25) with the SSCP model; (*a*, *b*) viscous mode, (*c*, *d*) heat-flux mode, (*e*, *f*) mass-flux mode, all normalized with the corresponding maximum DNS value.

data (figures 13*c* and 13*e*). Among different MGRD models, the best estimates are consistently obtained with MGRD-FOC. These results confirm those of § 6.2.1 that the MGRD-SOC is not as successful as the MGRD-FOC and further show that MGRD-NPC is considerably inferior to an MGRD model with a p correction, definitely assigning the success of the MGRD-FOC to the Taylor series model for $\nabla[\overline{p(\phi)} - p(\overline{\phi})]$.

For the GRD and SSCP models, the time evolution of g_{visc}, g_{temp} and g_{mass} are illustrated in figures 13(*b*), 13(*d*)and 13(*f*), respectively. After $t^\star = 70$, g_{visc} is overestimated for both the SSCP and GRDA-IC25 models, while it is underestimated with the GRDA-IC0 model. Although the SSCP and GRDA-IC25 models predict g_{visc} and g_{temp} equally well, the SSCP model gives a much better prediction for g_{mass}. Considering that for these type of flows g_{tot} is dominated by g_{mass}, the SSCP model is best overall.

7. Summary and conclusions

An *a posteriori* LES study has been conducted to identify the most promising SGS models for predicting fluid disintegration of two counterflow moving fluids and binary-fluid mixing at pressures initially higher than the critical pressure of either fluid. The LES governing equations consist of the filtered original equations for conservation of mass, momentum, species and total energy coupled with a real-gas EOS. These equations were previously solved using DNS. The transport properties were functions of the thermodynamic variables. Following a previous *a priori* investigation (Selle *et al.* 2007), the SGS terms in the differential equations consist of two types: (i) the typical SGS-flux terms and (ii) a pressure correction in the momentum equation accounting for the non-negligible difference between the filtered pressure and the pressure computed as a function of the filtered flow field. The second type of SGS term is the direct result of the strong EOS nonlinearity leading to the existence of HDGM regions in the flow having a complex small-scale structure.

The configuration was that of a three-dimensional mixing layer with initially heptane in the lower stream and nitrogen in the upper stream, and the DNS followed, for each realization, the evolution of the layer from an initial laminar state to a transitional state. The LESs were carried out with the same numerical discretization and time advancement numerical scheme as the DNSs. All LESs were conducted up to the same non-dimensional simulation time as the DNS, and the CPU time up to the DNS transitional state was considerably smaller than that of the DNS. Several types of LES models were assessed, all of which were compared with the FC-DNS: filtered to remove the small scales and coarsened to retain only the LES nodes. The FC-DNS represents an ideal, generally not achievable, LES. The three SGS-flux models assessed were the SM, the GR and the SS models. Two pressure-correction models were assessed. The first model relied on the first-order Taylor series expansion of the filtered pressure, and being the best quantitative approximation according to Taylor series concepts when using only one series term, it was used for all but one of the LESs. The second model was based on the second-order term of the Taylor expansion only, as the assumptions enabling utilization of the model based on this term had the consequence of nulling the first-order term; thus a combined first-order and second-order term model could not be used. The second-order term was modelled using variances which assumed one of the mathematical forms of the SGS-flux models. It turned out that the second-order term pressure correction was both more computationally intensive than the first-order one and a worse approximation of the FC-DNS. Thus the first-order Taylor expansion model was otherwise used.

Constant-coefficient SGS-flux models with coefficient values obtained at the transitional time in the *a priori* study were first evaluated in the LES, without or with the pressure correction model. Among models devoid of pressure correction, the SM model was overly dissipative, which resulted in lack of resolved small-scale structure; hence, it had a reasonable, although exaggerated, rendition of the pressure field. At the other extreme was the GR model which displayed small-scale structure, but the regions of low and high pressure were misplaced. The SS model was the most successful in that it combined small-scale structure and a reasonable, although understated, pressure field. The utilization of the pressure-correction model improved the morphology of the pressure field for the SM model, but the lack of resolved small-scale structure was still evident. The GR model benefitted most from the pressure correction in that the low- and high-pressure regions were now correctly placed, but the lowest pressure in the vortex core was still not reproduced. The most successful model was the one that combined the SS and pressure correction, as the morphology of the flow was closer to that of the FC-DNS than for the SS model with no pressure correction.

The good performance of the SS model motivated the evaluation of dynamic models, since they rely on the same underlying concept. Several dynamic models were assessed, including two mixed models utilizing the SM model in conjunction with either the GR or the SS model. Unlike in typical LES using mixed models, these combinations were not used to provide numerical stability to the computations (indeed, several LESs were successfully conducted using only the GR or the SS model) but to combine the good complementary predictions from each of the SM and GR or the SS model. The backscatter capability of the GR and SS models was also considered a potential asset in reproducing the FC-DNS transitional state. These mixed models were compared with the FC-DNS together with an SM-dynamic model and three GR-dynamic models. In one dynamic GR model LES, the computations were started at the time of the DNS IC. In another GR-dynamic model LES, the computation was initiated at a time past the DNS IC, so as to avoid the initial transients which made the pressure-correction term rival in magnitude the leading-order term in the momentum equation. Finally in the third dynamic GR model LES, the coefficients of the SGS-flux models were computed by domain averaging, whereas in all other LES with the GR or other SGS-flux models, it was computed by averaging in homogeneous planes. Among dynamic models, the SM-dynamic model was clearly the worst in all respects. The GR-dynamic model with the IC past the DNS transients was overall the best in terms both of the evolution of the global quantities and of flow visualizations at the transitional state of the DNS. Among all other models, the MGRD model was the best at duplicating the pressure but was not as adept as the GR-dynamic alone at reproducing the small-scale structure; the deficiency of the MGRD model was due to the presence of the SM model with its overly dissipative characteristics. An inquiry into the velocity-fluctuation-based spectra of dynamic models revealed that while MGRD reached transition at the DNS transitional time, neither SMD nor MSSD did so, and each furthermore underestimated the energy in the largest scales. The spectra examination showed that while all GR-dynamic model LESs reached transition at the DNS transitional time, they slightly overestimated the energy in the largest scales. Thus, the strategy of using mixed models to offset deficiencies from individual SGS models and instil small-scale duplication capabilities proved somewhat successful (tested also with DNS realizations other than those for which the models were developed); however, the lack of temporal equivalence

with the FC-DNS in achieving the transitional state makes some SM-based models problematic if both temporal and spatial equivalence with the FC-DNS are the goal, although the models may be considered acceptable for statistical equivalence. An alternate strategy to achieve LES/FC-DNS temporal and spatial equivalence was choosing an appropriate time for initiating the LES and avoiding the utilization of SM-based models. For practical applications, this would mean that measurements past initial transients should be used for initiating LES. Clearly, the LES dynamic models present many options for conducting simulations, and it is the privilege and responsibility of the user to choose the option which best suits the LES goal.

To further probe the capabilities of the LES models, an inquiry was made into the ability of the LES to reproduce the FC-DNS irreversible entropy production, which is the dissipation. Not only is this information of scientific interest, as the dissipation has special characteristics uniquely related to the flow (Okong'o & Bellan 2002*b*, 2004*a*), but this information also has practical applications in that numerical methods have been based on entropy conservation (Honein & Moin 2004). Examined here were the contribution from each of its three modes: viscous, heat flux and species mass flux. The mass-flux mode being known to dominate the dissipation for these high-pressure conditions (Okong'o & Bellan 2002*b*; Okong'o, Harstad & Bellan 2002), the constant-coefficient SS model in conjunction with the pressure correction proved best.

As a general observation, at the transitional-Reynolds-number values of this study the pressure correction improved the LES predictions, but an even more considerable improvement is expected at higher Reynolds numbers, since experimental observations (see examples in Selle *et al.* 2007) show that the gradients in the HDGM regions can have a value by an order of magnitude higher than those in the present DNS database.

This study addressed only one of the additional (to the SGS flux) SGS models found necessary to reproduce in LES the features of the supercritical-pressure FC-DNS. For the OH system an equivalent term, the divergence of the difference between the filtered heat flux and the heat flux computed from the filtered solution, was found of leading order in the energy equation. A future study will address the *a posteriori* modelling of that term. For other species combinations, e.g. OHe, both the pressure and heat flux correction terms are apparently necessary (Selle *et al.* 2007), and a future *a posteriori* study will examine their impact on the fidelity of the LES compared with the FC-DNS.

Finally, the general methodology introduced here of using (other than SGS-flux) SGS models to enable the LES computation of single-phase flows having strong localized gradients could be extended to other applications.

This work was conducted at the Jet Propulsion Laboratory (JPL), California Institute of Technology (Caltech), and was sponsored by the Air Force Office of Scientific Research (AFOSR) under the direction of Dr Julian Tishkoff, serving as technical director, under an agreement with the National Aeronautics and Space Administration, and under an AFOSR grant to Caltech under the technical direction of Drs Mitat Birkan, Douglas Talley (of Edwards Air Force Research Laboratories, or Edwards AFRL), Timothy Edwards and Campbell Carter (both of Wright Patterson AFRL). We also wish to thank Dr Nora Okong'o for very helpful discussions on numerical techniques. The computational resources were provided by the JPL Supercomputing Center.

HN600	x_1 momentum				x_2 momentum				x_3 momentum			
t^*	25	50	100	135	25	50	100	135	25	50	100	135
$\frac{\partial}{\partial x_j}(\bar{\rho}\tilde{u}_i\tilde{u}_j)$	5.87	11.69	19.37	20.81	2.72	7.70	13.87	14.61	1.17	4.60	10.03	13.08
$\frac{\partial}{\partial x_i}[p(\bar{\phi})]$	4.39	11.61	14.73	13.19	11.02	17.71	20.92	18.38	8.88	14.73	18.70	16.07
$\frac{\partial}{\partial x_i}[\Delta(\bar{p})]$	2.44	9.12	11.13	9.93	10.83	16.54	17.20	15.65	8.83	13.91	17.17	13.82

$\Delta(\bar{f}) \equiv \overline{f(\phi)} - f(\bar{\phi})$

TABLE 8. Activity (r.m.s.) of the three leading-order terms in the momentum equation at t^*=25, 50, 100, 135 from the HN600 DNS. The computation was made with $\bar{\Delta} = 8\Delta x_{DNS}$. Units are 10^6 N m^{-3}.

Appendix A. Influence of LES ICs for constant-coefficient SGS-flux models

The ICs are subject to choice in LES, and there is still no consensus on an optimal such set. Here we wish to explore two IC aspects, namely whether it is best to choose the FC-DNS or CF-DNS as the IC, as discussed in §4, and whether it is more appropriate to use as LES IC the FC-DNS at $t^* = 0$ or at a later DNS time station, as also discussed in §4. The latter inquiry can be understood by examining table 8 listing the magnitude (computed using the domain root mean square, or r.m.s., which is related to the L2 norm) of the leading first three terms in the momentum equation using the DNS database and $\overline{\Delta} = 8\Delta x_{DNS}$, corresponding to the filter width used in the present LES. The listed magnitude is at $t^* = 25$, 50, 100 and 135. Examination of the table shows that the LES assumption on ∇p, namely the term $\nabla[\overline{p(\phi)} - p(\bar{\phi})]$, which motivated the p-correction model, is one of the two leading-order terms in the x_2 and x_3 components of the momentum equation at $t^* = 25$, and only at $t^* = 50$ it seems to be very slightly smaller than (although of the same order of magnitude as) the leading, $\nabla[p(\bar{\phi})]$, term. It is thus legitimate to doubt whether an approximation, such as embedded in the p correction, would be able to recover at the early times the prominent features of a flow dominated by this $\nabla[\overline{p(\phi)} - p(\bar{\phi})]$ effect. The success obtained with constant-coefficient LES starting from $t^* = 0$, as shown in §6.1, is testimonial to the robustness and accuracy of the p-correction model, but here we show that those were conservative results and that a much better agreement with the FC-DNS at $t^* = 135$ can be obtained if the LES is initiated with the FC-DNS at $t^* = 50$. This choice of IC at a time later than the DNS $t^* = 0$ time station was also the approach of Geurts & Frohlich (2002) even though that flow did not display the strong non-uniformities manifested here in the HDGM regions.

Figure 14 compares the time evolution of global quantities obtained from the DNS and the LES using different ICs along with FC-DNS. All LES runs are performed with the GRCP model using the coefficient of (6.2) and reveal the following. The $\delta_m/\delta_{\omega,0}$ of the LES initiated from CF-DNS conditions (CFDNS-IC0) follows the FC-DNS up to $t^* = 60$ after which it departs from the template and has slightly better agreement with it at $t^* = 135$ compared with the LES run initiated from FC-DNS conditions (FCDNS-IC0). In comparison, $\delta_m/\delta_{\omega,0}$ of the LES started from $t^* = 50$ (FCDNS-IC50) agrees considerably better with the FC-DNS. Similarly, E_K/E_0 obtained with both CFDNS-IC0 and FCDNS-IC50 agrees better with the FC-DNS data up to $t^* = 120$ when compared with that obtained with FC-DNS-IC0. As for the vorticity activity, FCDNS-IC0 and CFDNS-IC0 perform similarly, and they are inferior to FCDNS-IC50.

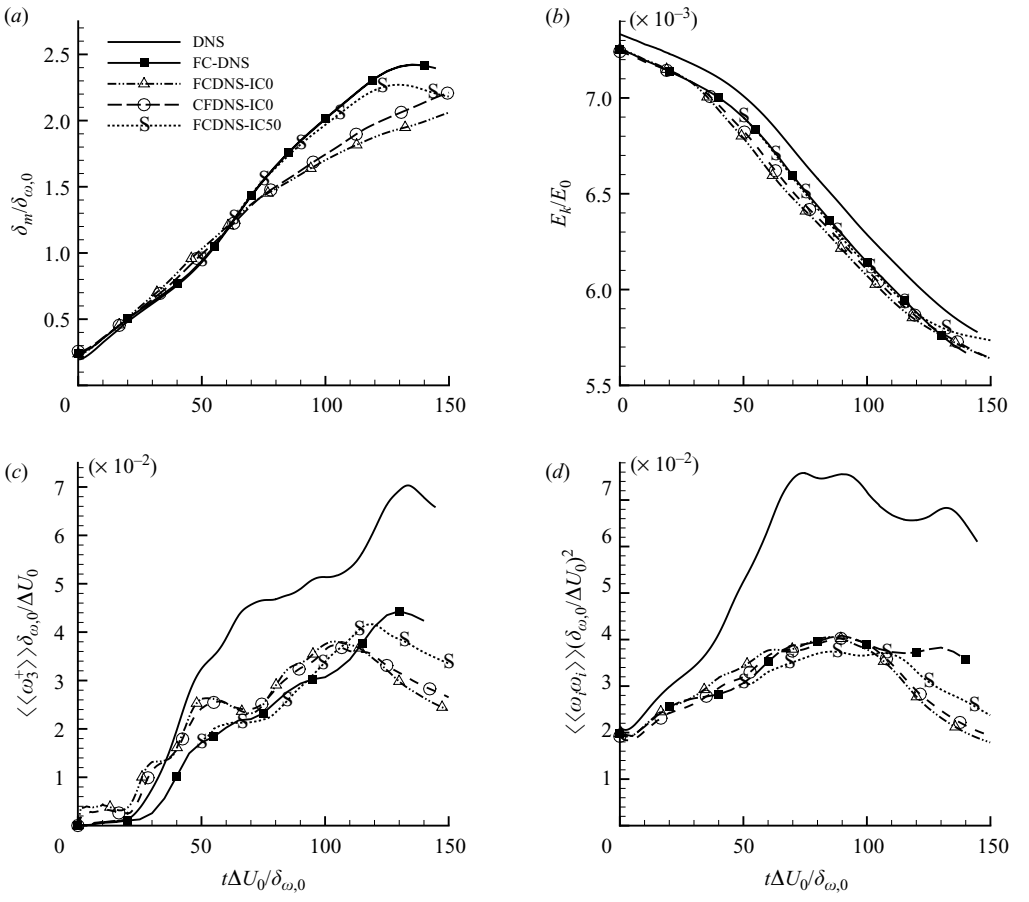

FIGURE 14. Time evolution of non-dimensional global quantities for HN600: (*a*) $\delta_m/\delta_{\omega,0}$, (*b*) E_K/E_0, (*c*) $\langle\langle\omega_3^+\rangle\rangle\delta_{\omega,0}/\Delta U_0$ and (*d*) $\langle\langle\omega_i\omega_i\rangle\rangle(\delta_{\omega,0}/\Delta U_0)^2$ for DNS, FC-DNS, LES initiated from FC-DNS at $t^* = 0$ (FCDNS-IC0 with GRCP), CF-DNS at $t^* = 0$ (CFDNS-IC0 with GRCP) and FC-DNS at $t^* = 50$ (FCDNS-IC50 with GRCP).

Companion flow visualizations of $|\nabla\rho|$, p/p_0 and Y_h, (not shown) for LES initiated from the FC-DNS conditions at $t^* = 0$, from the CF-DNS conditions at $t^* = 0$ and from the FC-DNS conditions at $t^* = 50$, along with the FC-DNS at $t^* = 135$, show that considering all three variables, FCDNS-IC50 produces the best match with the FC-DNS data. Also, p/p_0 and Y_h are slightly better predicted with CFDNS-IC0 than with FCDNS-IC0.

Thus, the results show that utilizing ICs at a time station past the largest pressure-gradient transients yields much more accurate LES results.

Appendix B. Influence of the grid size

The concept of grid convergence does not apply to LES because discretization errors, numerical errors and modelling errors are all intertwined as explained by Vreman, Geurts & Kuerten (1996*a*) and Meyer *et al.* (2003). For example, the discretization error depends not only on the numerical method but also on the choice of $\overline{\Delta}/\Delta x_{LES}$. What we wish to determine here is whether a finer LES grid

would be more beneficial in computing the HDGM regions, and if so, to what extent and at what cost. To investigate the grid choice, a finer-grid LES, with the grid having twice as many nodes in each direction, is performed, i.e. $\Delta x_{LES} = 2\Delta x_{DNS}$. Since $\overline{\Delta}/\Delta x_{LES}$ is kept at the same value, the filter size, $\overline{\Delta} = 4\Delta x_{DNS}$, is half of what it was for the coarse grid. This constant $\overline{\Delta}/\Delta x_{LES}$ strategy is preferred because the SGS p-correction model through the Taylor expansion is based on the assumption that $(\phi - \bar{\phi})$ is small. The GRCP model coefficient for the finer grid LES is the calibrated value at the DNS transitional time of 0.1346 (Selle *et al.* 2007). All calculations were started from the FC-DNS at $t^* = 0$.

The time evolution of global quantities (not shown) indicates that the fine grid solution has a better agreement with the filtered DNS in all four plots. For the fine-grid LES, both $\delta_m/\delta_{\omega,0}$ and E_K/E_0 decay are slightly overpredicted, and $\langle\langle\omega_3^+\rangle\rangle\delta_{\omega,0}/\Delta U_0$ and $\langle\langle\omega_i\omega_i\rangle\rangle(\delta_{\omega,0}/\Delta U_0)^2$ are slightly underpredicted. For comparison, the No Model LES solution with the finer grid yields reasonably good agreements with the DNS, indicating that there is no need for LES and SGS modelling at this resolution. Thus, at the fine resolution, the SGS model only represents an unnecessary computational overhead. No LES grid coarser than $\Delta x_{LES} = 4\Delta x_{DNS}$ (e.g. $\Delta x_{LES} = 8\Delta x_{DNS}$) has been attempted, since the accuracy of the initial profiles significantly deteriorates on coarser grids. The grid resolution is also dictated by the thickness of the HDGM regions

When analysing the $|\nabla\rho|$, p/p_0 and Y_h contour plots for the coarse grid and fine grid LES and for FC-DNS at the two $\overline{\Delta}$ widths corresponding to the coarse and fine grids (not shown), one observes that the FC-DNS at both fine and coarse filters displays $|\nabla\rho|$ and Y_h having very dense contour lines in narrow bands; this detail is not captured with the coarse-grid LES but is reproduced by the finer-grid LES.

Finally, the computational time requirement of the finer-resolution LES is 160 CPU hours computed as the aggregate over 64 parallel processors on an SGI Altix 3000 system. This is approximately 16 times more than that for the equivalent coarse-grid LES. Ultimately, the model user has the privilege of determining the grid size according to the objectives of the application.

Appendix C. Model evaluation using several realizations of the DNS database

Compared with HN600, the DNS realization HN500 displays HDGM regions which are thicker and more extensively spread over the domain, and the peak $|\nabla\rho|\delta_{\omega,0}/\Delta\rho_0$ (where $\Delta\rho_0 = \rho_1 - \rho_2$) at t^*_{tr} is smaller in magnitude. The DNS of HN800 exhibits a character different from HN500 or HN600 in that the peak $|\nabla\rho|\delta_{\omega,0}/\Delta\rho_0$ at t^*_{tr} is approximately twice that of HN500 and 60 % larger than that of HN600, and also because the HDGM regions are concentrated in a small region of the domain, and are smooth and relatively thin. However, $Re_{m,tr}$ for HN800 is similar to that of HN500 and only slightly smaller than that of HN600 (see table 3). Utilizing SSCP and MGRD in the LES to recover the FC-DNS for these two different realizations is a reasonable test of the LES model approach.

The LES conducted with each SSCP and MGRD required 13 CPU hours for HN500 and 12 CPU hours for HN800. In the SSCP model, the coefficient is taken to be the calibrated value obtained at the DNS transition time, $C_{SS} = 0.6260$ and $C_{SS} = 0.5870$ for HN500 and HN800, respectively; and $\hat{\Delta}/\bar{\Delta} = 2$, as for the HN600 LES. The global quantities $\delta_m/\delta_{\omega,0}$, E_K/E_0 $\langle\langle\omega_3^+\rangle\rangle\delta_{\omega,0}/\Delta U_0$ and $\langle\langle\omega_i\omega_i\rangle\rangle(\delta_{\omega,0}/\Delta U_0)^2$ presented in figure 15 show that the two LES models generally flank the corresponding FC-DNS, with SSCP generally overestimating and MGRD generally underestimating

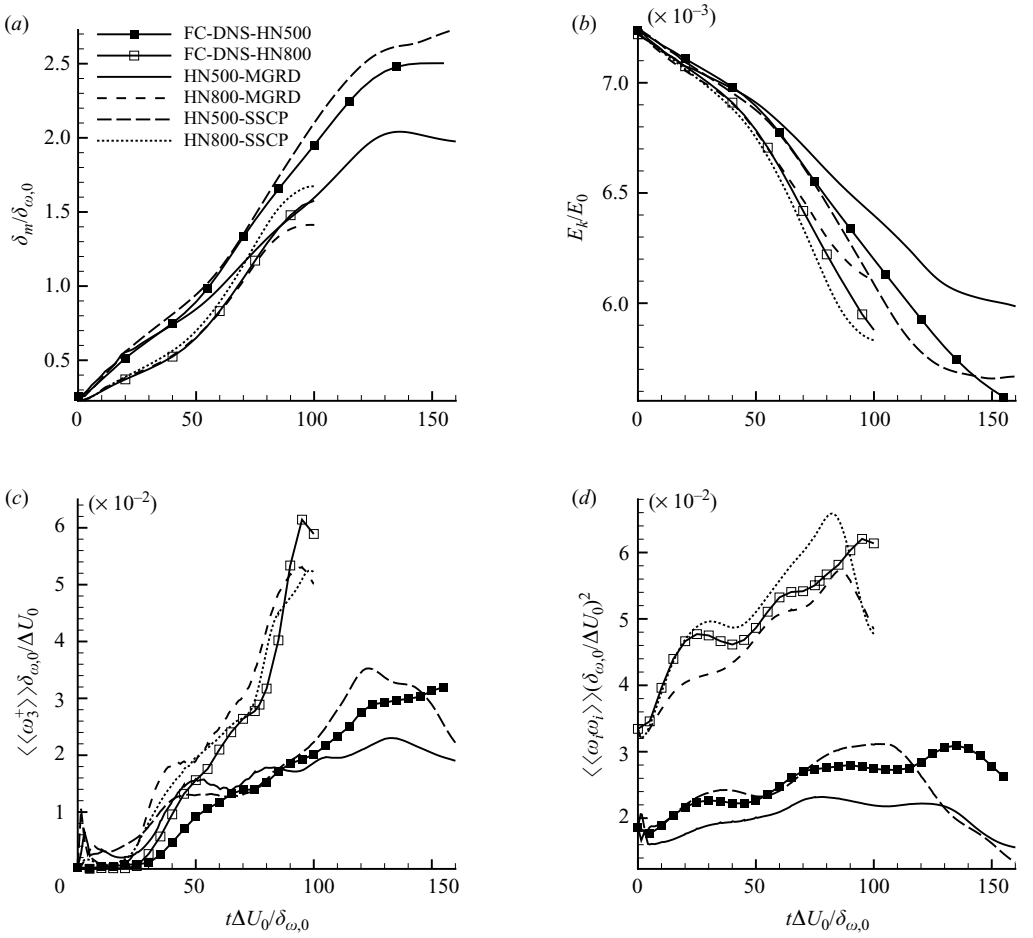

FIGURE 15. Time evolution of non-dimensional global quantities for HN500 and HN800: (*a*)$\delta_m/\delta_{\omega,0}$, (*b*) E_K/E_0, (*c*) $\langle\langle\omega_3^+\rangle\rangle\delta_{\omega,0}/\Delta U_0$ and (*d*) $\langle\langle\omega_i\omega_i\rangle\rangle(\delta_{\omega,0}/\Delta U_0)^2$ for FC-DNS and two LES models (MGRD and SSCP) both including the FOC model.

the target FC-DNS and with the SSCP consistently being a better approximation of the ideal objective. Of note is the tandem timewise path of SSCP and the FC-DNS for both $\langle\langle\omega_3^+\rangle\rangle\delta_{\omega,0}/\Delta U_0$ and $\langle\langle\omega_i\omega_i\rangle\rangle(\delta_{\omega,0}/\Delta U_0)^2$ until close to transition. The diverging MGRD LES from the FC-DNS is the result of the SM model contribution which, having dissipated energy excessively, makes the LES unable to sustain the small-scale necessary to promote further layer growth and the generation of vortical activity. Although the SSCP model agrees better with the FC-DNS template for all four quantities, it yields a larger positive vorticity peak for the HN500 case at the beginning of the simulation.

Complementary information in flow visualizations (not shown) of $|\nabla\rho|$, p/p_0 and Y_h comparing the LES with the FC-DNS indicates that for HN500 all $|\nabla\rho|$, p/p_0 and Y_h are better reproduced by MGRD than by SSCP. Particularly, for the SSCP model there are Y_h regions in the mixing layer in which fluid from the upper stream has been entrained and has not mixed with adjacent fluid, an occurrence which is not supported by the FC-DNS results. However, for HN800, the SSCP model is clearly

better duplicating than MGRD all $|\nabla\rho|$, p/p_0 and Y_h, including the entrained fluid from the upper stream which is being stirred into the mixing layer.

This necessarily limited application of the LES models to other realizations, spanning a range of *Re* values, brings some additional perspective and shows the models' robustness.

REFERENCES

Bardina, J., Ferziger, J. & Reynolds, W. 1980 Improved subgrid scale models for large eddy simulation. *Paper* 80-1357. AIAA.

Bellan, J. 2006 Theory, modelling and analysis of turbulent supercritical mixing. *Combust. Sci. Technol.* **178**, 253–281.

Berselli, L. C., Iliescu, T. & Layton, W. J. 2006 *Mathematics of Large Eddy Simulation of Turbulent Flows.* Springer.

Chehroudi, B., Talley, D. & Coy, E. 1999 Initial growth rate and visual characteristics of a round jet into a sub- to supercritical environment of relevance to rocket, gas turbine and diesel engines. *Paper* 99-0206. AIAA.

Chow, F. K. & Moin, P. 2003 A further study of numerical errors in large-eddy simulations. *J. Comput. Phys.* **184**, 366–380.

Clark, R., Ferziger, J. & Reynolds, W. 1979 Evaluation of subgrid-scale models using an accurately simulated turbulent flow. *J. Fluid Mech.* **91** (1), 1–16.

Germano, M., Piomelli, U., Moin, P. & Cabot, W. 1991 A dynamic subgrid-scale eddy viscosity model. *Phys. Fluids* A **3** (7), 1760–1765.

Geurts, B. J. & Frohlich, J. 2002 A framework for predicting accuracy limitations in large-eddy simulation. *Phys. Fluids* **14** (6), L41–L44.

Ghosal, S. 1996 An analysis of numerical errors in large-eddy simulations of turbulence. *J. Comput. Phys.* **125**, 187–206.

Hannoun, I. A., Fernando, H. J. S. & List, E. J. 1988 Turbulence structure near a sharp density interface. *J. Fluid Mech.* **189**, 189–209.

Harstad, K. & Bellan, J. 1998 Isolated fluid oxygen drop behaviour in fluid hydrogen at rocket chamber pressures. *Intl J. Heat Mass Transfer* **41**, 3537–3550.

Harstad, K. & Bellan, J. 2000 An all-pressure fluid-drop model applied to a binary mixture: heptane in nitrogen. *Intl J. Multiphase Flow* **26** (10), 1675–1706.

Harstad, K., Miller, R. S. & Bellan, J. 1997 Efficient high-pressure state equations. *AIChE J.* **43** (6), 1605–1610.

Hirshfelder, J., Curtis, C. & Bird, R. 1964 *Molecular Theory of Gases and Liquids.* John Wiley.

Honein, A. E. & Moin, P. 2004 Higher entropy conservation and numerical stability of compressible turbulence simulations. *J. Comput. Phys.* **201**, 531–545.

Keizer, J. 1987 *Statistical Thermodynamics of Nonequilibrium Processes.* Springer.

Kennedy, C. & Carpenter, M. 1994 Several new numerical methods for compressible shear layer simulations. *Appl. Numer. Math.* **14** 397–433.

Leboissetier, A., Okong'o, N. & Bellan, J. 2005 Consistent large-eddy simulation of a temporal mixing layer laden with evaporating drops. Part 2. *A posteriori* modelling. *J. Fluid Mech.* 523, 37–78.

Lilly, D. 1992 A proposed modification of the Germano subgrid-scale closure method. *Phys. Fluids* A **4** (3), 633–635.

Liu, S., Meneveau, C. & Katz, J. 1994 On the properties of similarity subgrid-scale models as deduced from measurements in a turbulent jet. *J. Fluid Mech.* **275**, 83–119.

Mayer, W., Schik, A., Schweitzer, C. & Schaffler, M. 1996 Injection and mixing processes in high pressure LOX/GH2 rocket combustors. *Paper* 96-2620. AIAA.

Mayer, W., Ivancic, B., Schik, A. & Hornung, U. 1998 Propellant atomization in LOX/GH2 rocket combustors. *Paper* 98-3685. AIAA.

Meyer, J., Geurts, B. J. & Baelmans, M. 2003 Database analysis of errors in large-eddy simulation. *Phys. Fluids* **15** (9), 2740–2755.

Miller, R., Harstad, K. & Bellan, J. 2001 Direct numerical simulations of supercritical fluid mixing layers applied to heptane-nitrogen. *J. Fluid Mech.* **436**, 1–39.

Moin, P., Squires, K., Cabot, W. & Lee, S. 1991 A dynamic subgrid-scale model for compressible turbulence and scalar transport. *Phys. Fluids* **3** (11), 2746–2757.

Moser, R. & Rogers, M. 1991 Mixing transition and the cascade to small scales in a plane mixing layer. *Phys. Fluids* A **3** (5), 1128–1134.

Moser, R. & Rogers, M. 1993 The three-dimensional evolution of a plane mixing layer: pairing and transition to turbulence. *J. Fluid Mech.* **247**, 275–320.

Muller, S. M. & Scheerer, D. 1991 A method to parallelize tridiagonal solvers. *Par. Comput.* **17**, 181–188.

Oefelein, J. C. 2005 Thermophysical characteristics of shear-coaxial LOX-H_2 flames at supercritical pressure. *Proc. Combust. Inst.* **30**, 2929–2937.

Oefelein, J. C. & Yang, V. 1998 modelling high-pressure mixing and combustion processes in liquid rocket engines. *J. Propul. Power* **14**, 843–857.

Okong'o, N. & Bellan, J. 2000 Entropy production of emerging turbulent scales in a temporal supercritical n-heptane/nitrogen three-dimensional mixing layer. *Proc. Combust. Inst.* **28**, 497–504.

Okong'o, N. & Bellan, J. 2002*a* Consistent boundary conditions for multicomponent real gas mixtures based on characteristic waves. *J. Comput. Phys.* **176**, 330–344.

Okong'o, N. & Bellan, J. 2002*b* Direct numerical simulation of a transitional supercritical binary mixing layer: heptane and nitrogen. *J. Fluid Mech.* **464**, 1–34.

Okong'o, N. & Bellan, J. 2003 Real gas effects of mean flow and temporal stability of binary-species mixing layers. *AIAA J.* **41** (12), 2429–2443.

Okong'o, N. & Bellan, J. 2004*a* Consistent large eddy simulation of a temporal mixing layer laden with evaporating drops. Part 1. Direct numerical simulation, formulation and *a priori* analysis. *J. Fluid Mech.* **499**, 1–47.

Okong'o, N. & Bellan, J. 2004*b* Turbulence and fluid-front area production in binary-species, supercritical, transitional mixing layers. *Phys. Fluids* **16** (5), 1467–1492.

Okong'o, N., Harstad, K. & Bellan, J. 2002 Direct numerical simulations of O_2/H_2 temporal mixing layers under supercritical conditions. *AIAA J.* **40** (5), 914–926.

Oschwald, M. & Schik, A. 1999 Supercritical nitrogen free jet investigated by spontaneous Raman scattering. *Exp. Fluids* **27**, 497–506.

Oschwald, M., Schik, A., Klar, M. & Mayer, W. 1999 Investigation of coaxial LN2/GH2-injection at supercritical pressure by spontaneous Raman scattering. *Paper* AIAA-99-2887. AIAA.

Papamoschou, D. & Roshko, A. 1988 The compressible turbulent shear layer: an experimental study. *J. Fluid Mech.* **197**, 453–477.

Pope, S. B. 2004 Ten questions concerning the large-eddy simulation of turbulent flows. *New J. Phys.* **6**, 35–59.

Prausnitz, J., Lichtenthaler, R. & de Azevedo, E. 1986 *Molecular Thermodynamics for Fluid-Phase Equilibrium.* Prentice-Hall.

Pruett, C., Sochacki, J. & Adams, N. 2001 On Taylor-series expansions of residual stress. *Phys. Fluids* **13** (9), 2578–2589.

Sarman, S. & Evans, D. J. 1992 Heat flux and mass diffusion in binary Lennard-Jones mixtures *Phys. Rev.* A **45** (4), 2370–2379

Segal, C. & Polikhov, S. 2008 Subcritical to supercritical mixing. *Phys. Fluids* **20**, 052101-7.

Selle, L. C., Okong'o, N. A., Bellan, J. & Harstad, K. G. 2007 modelling of subgrid scale phenomena in supercritical transitional mixing layers: an *a priori* study. *J. Fluid Mech.* **593**, 57–91.

Smagorinksy, J. 1963 General circulation experiments with the primitive equations. Part 1. basic experiments. *Mon. Weather Rev.* **91**, 99–164.

Smagorinksy, J. 1993 Some historical remarks on the use of nonlinear viscosities. In *Large Eddy Simulation of Complex Engineering and Geophysical Flows* (ed. B. Galperin & S. Orszag), chapter 1, pp. 3–36. Cambridge University Press.

Speziale, C. G., Erlebacher, G., Zang, T. A. & Hussaini, M. Y. 1988 The subgrid-scale modelling of compressible turbulence. *Phys. Fluids* A **31**, 940–942.

Tennekes, H. & Lumley, J. L. 1989 *A First Course in Turbulence*. MIT Press.

Vreman, B., Geurts, B. & Kuerten, H. 1996*a* Comparison of numerical schemes in large-eddy simulation of the temporal mixing layer. *Intl J. Num. Meth. Fluids* **22**, 297–311.

Vreman, B., Geurts, B. & Kuerten, H. 1996*b* Large eddy simulation of the temporal mixing layer using the Clark model. *Theoret. Comput. Fluid Dyn.* **8**, 309–324.

Vreman, B., Geurts, B. & Kuerten, H. 1997 Large-eddy simulation of the turbulent mixing layer. *J. Fluid Mech.* **339**, 357–390.

Yoshizawa, A. 1986 Statistical theory for compressible turbulent shear flows, with the application to subgrid modelling. *Phys. Fluids* **29** (7), 2152–2164.

Zang, Y., Street, R. L. & Koseff, J. R. 1993 A dynamic mixed subgrid-scale model and its application to turbulent recirculating flows. *Phys. Fluids* A **5**, 3186–3196.

Zong, N., Meng, H., Hsieh, S.-Y. & Yang, V. 2004 A numerical study of cryogenic fluid injection and mixing under supercritical conditions. *Phys. Fluids* **16** (12), 4248–4261.